Remote Sensing of Environment 304 (2024) 114059

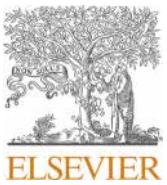

Contents lists available at ScienceDirect

Remote Sensing of Environment

journal homepage: www.elsevier.com/locate/rse

Temporal decorrelation of C-band radar data over wheat in a semi-arid area using sub-daily tower-based observations

Nadia Ouaadi [a,b,*], Lionel Jarlan [a], Ludovic Villard [a], Adnane Chakir [c,d], Saïd Khabba [c,e], Pascal Fanise [a], Mohamed Kasbani [a], Zoubair Rafi [c], Valerie Le Dantec [a], Jamal Ezzahar [e,f], Pierre-Louis Frison [d]

[a] CESBIO, University of Toulouse, IRD/CNRS/UPS/CNES, Toulouse, France
[b] GMME/SURFACE, Meteo-France/CNRM, Toulouse, France
[c] LMFE, Faculty of Sciences Semlalia, Cadi Ayyad University, Marrakech, Morocco
[d] LaSTIG, Gustave Eiffel University, Paris, France
[e] CRSA, Mohammed VI Polytechnic University, Ben Guerir, Morocco
[f] MISCOM, National School of Applied Sciences, Safi, Morocco.

ARTICLE INFO

Edited by Marie Weiss

Keywords:
Temporal coherence
C-band
Diurnal cycle
Seasonal cycle
Evapotranspiration
Irrigation
Dew
Wheat
Phenological stages
Semi-arid region

ABSTRACT

Recent studies have shown that radar temporal coherence over tropical and boreal forests undergoes a diurnal cycle as a result of a combined effect of the wind-induced motion of scatterers and of the change and displacement of water within the plant in response to the transpiration process. Within this context, the objective of this paper is to investigate, for the first time, the diurnal cycle of temporal coherence over wheat crops in relation to its development and physiological functioning throughout the agricultural season. A ground-based experiment was installed in Morocco, targeting a wheat field during the 2020 agricultural season. The radar system, essentially based on a Vector Network Analyzer (VNA) connected to 6C-band antennas installed at the top of a 20 m tower, has enabled quad-polarimetric acquisitions every 15 min. In parallel, evapotranspiration, soil moisture and meteorological variables are automatically measured in addition to above-ground biomass and vegetation water content collected during field campaigns. The results show that the temporal coherence with a 15 min baseline follows a marked diurnal cycle characterized by variable amplitude according to the phenological stage, with high values during the night, a significant morning drop to reach the lowest values in the late afternoon followed by an increase to recover the high nighttime values. The rate of the drop at dawn is shown to be related to the increase of evapotranspiration ($r = 0.80$ at VV polarization) when the wheat is covering the soil and the transpiration dominate the evapotranspiration process. This supports the assumption of a physiological effect related to water movement entailing a decorrelation. By contrast, the daily minimum of temporal coherence occurring in the late afternoon correlates well to the daily maximum of wind ($r = 0.7$). Interestingly enough, the amplitude of the diurnal cycle exhibit a marked seasonal evolution characterized by an increase of 85% from tillering to maturity in relation to the wheat development. At the early start of the season when the soil is almost bare, irrigation events impact slightly the diurnal cycle of temporal coherence. Likewise, it is shown that the presence of dew in the early morning has led to a decrease of the decorrelation rate. Temporal coherence dynamic has also been investigated for longer baselines up to 22 days. Results indicate a stronger decorrelation than what has been observed on tropical and boreal forests by previous studies with values below 0.4 for baselines above 2 days. Taken together, the results of this work demonstrate the unique potential of sub-daily C-band data for monitoring crop water status by future geostationary radar missions such as Hydroterra.

1. Introduction

Water resource management is a critical issue worldwide. Water consumption is continuously increasing especially in the agricultural sector which is the major consumer with >70% of available water. While about two billion people around the world are already suffering

* Corresponding author at: CESBIO, University of Toulouse, IRD/CNRS/UPS/CNES, Toulouse, France.
E-mail address: nadia.ouaadi@gmail.com (N. Ouaadi).

https://doi.org/10.1016/j.rse.2024.114059
Received 27 May 2023; Received in revised form 14 February 2024; Accepted 15 February 2024
Available online 22 February 2024

from water scarcity (Leal Filho et al., 2022; Stringer et al., 2021; UNICEF, 2019), irrigated land is steadily increasing (Foley et al., 2011; MedECC, 2020) due to decreasing precipitation and increasing evapotranspiration, which are in turn attributed to climate change, especially in semi-arid regions (MedECC, 2020). Adaptations and mitigation under these conditions require optimal and efficient crop water management methods to ensure food security for the growing population while preserving water resources. This requires an understanding of the vegetation water cycle to monitor and optimize its water requirements.

Vegetation water requirements and stress can ideally be controlled using in situ measurements, such as measuring evapotranspiration and soil moisture can indicate when vegetation should be irrigated and how much is needed. Although accurate, such equipment and facilities are expensive and provide only local information (Allen et al., 2011). Remote sensing methods are preferred as they can provide information on a large scale and, in most cases, free of charge. Indeed, optical data are historically used to monitor vegetation by deriving indices from optical reflectance, but these methods only indicate the need for watering when vegetation is already impacted by water stress (Le Page et al., 2014). By contrast, thermal data is a powerful tool as surface temperature can be an indirect proxy for the vegetation's water status (Ihuoma and Madramootoo, 2017; Jackson et al., 1981; Stefan et al., 2015) when water is limiting. Nevertheless, with the sensors into orbit, there are no thermal observations combining both high spatial resolution with a high revisit time, and they are prone to atmospheric perturbation limiting their availability on cloudy regions.

Radar data, by contrast, have shown high potential for the monitoring of vegetation and of the underlying soil given their sensitivity to the water content of the target via its dielectric properties (Brakke et al., 1981; Ulaby et al., 1986; Van Emmerik et al., 2017). Indeed, the daily water cycle of the canopy is determined by the balance between water uptake from the soil and water loss through transpiration. For trees, it is characterized by a stem hydration from twilight to dawn followed by a loss of water in response to sapflow until late afternoon. Water availability is the main factor affecting this daily cycle. This daily alternance of water loss and rehydration is expected to affect the radar response. Indeed, at the sub-daily time scale, Mcdonald et al. (2002) found a diurnal cycle of the dielectric constant of a Spruce tree at P-band, with a maximum between 06 h and 09 h (a.m.) and a minimum between 15 h and 18 h. This corresponds to a high water content of the vegetation in the early morning at the end of the stem's hydration phase (Gates, 1991; Herzog et al., 1995).

The first studies that have witnessed a diurnal cycle of radar data were using the signal intensity (backscattering coefficient) since 80s (Birrer et al., 1982; Friesen et al., 2007; Frolking et al., 2011; Kunz and Long, 2005; Long and Skouson, 1996). Conversely, the temporal decorrelation, is studied rather on a seasonal scale using satellite radar sensors such as Sentinel-1 with a revisit time of 6 days. It has proven to be valuable and accurate for a wide range of vegetation-related applications, such as biophysical variable retrieval (Blaes and Defourny, 2003; Ouaadi et al., 2021; Villarroya-Carpio et al., 2022), classification (Mestre-Quereda et al., 2020) and evapotranspiration estimation (Ouaadi et al., 2023). Nevertheless, 6 days is not sufficient to monitor some physical processes that occur on a short time scale; hourly in the best cases. Higher temporal resolution of spaceborne radars should be achieved in the next decade, driven by the need of such resolution for large wide of applications from agronomy to meteorology. In parallel to commercial SAR imaging satellites (Capella Space, n.d; ICEYE, n.d), new mission projects are emerging, notably at ESA for geostationary missions that offer attractive new capabilities, especially high temporal resolution (Hu et al., 2021). For example, ESA's Hydroterra+ (the new iteration of Hydroterra (ESA, 2020)) C-band missions will be the first to make continuous measurements over Europe and Africa. The mission is designed to answer the most relevant questions related to improving the understanding of the rapid processes occurring over periods of a few hours.

Recently, sub-daily temporal coherence has been studied in tropical forests using ground-based experiments that are mainly conducted in preparation for the P-band BIOMASS mission (ESA, 2012) to be launched in 2024. The ground-based experiments allow obtaining data at high temporal frequencies, typically few minutes, which provides unique opportunities to investigate biophysical processes of vegetation in fine at sub-daily time scale. Indeed, Hamadi et al. (2014) and Albinet et al. (2016) have shown that the temporal coherence obtained from an L- and P- bands ground scatterometer experiment exhibits a diurnal cycle. This cycle is clearer and more important during dry periods, while the presence of precipitation disturbs the cycle (Hamadi et al., 2015) since precipitation disturbs the dielectric constant cycle (Mcdonald et al., 2002). Hamadi et al. (2014) have found that temporal coherence loss (decorrelation) during the day are associated with strong winds (>2.5 m/s), while the temporal coherence is high during the night when the wind is low. However, it is also possible that these differences between day and night are due to variations in water content and thus transpiration. Indeed, it has been shown in the literature that the loss of coherence (or decorrelation) is driven by (i) displacements of the scatterers, typically induced by wind and precipitation; (ii) changes of soil moisture or vegetation water content related to the physiological functioning of the plant impacting the dielectric constant of the target; and (iii) changes in the morphological properties of the medium due to its development (Lavalle et al., 2012).

Wind is known to be an important source of decorrelation (induces shifts of more than half the wavelength at C-band (El Idrissi Essebtey et al., 2019)). This has been demonstrated by direct measurements (Askne et al., 1997) but also by taking it into account in coherence models (Askne et al., 1997; Lavalle et al., 2012). It is worth mentioning here that the derivation of these models is based on assumptions related to the development and functioning of the vegetation. For example, Lavalle et al. (2012) built their model (temporal decorrelation model) for short and moderate temporal baselines assuming that vegetation characteristics such as height (development) and wave extinction (functioning) do not change between acquisitions. The development of vegetation leads to long-term temporal decorrelation. But during single day, this effect remains limited compared to the change in dielectric properties which should have a more significant impact on the signal. Indeed, it has been demonstrated by El Idrissi Essebtey et al. (2019) that transpiration is the main driver of the decrease in C-band temporal coherence at dawn given that the winds are close to zero over this time span. Later in the day, it was difficult to distinguish the effects of dielectric changes induced by water movement in trees and the effect of wind. However, these studies were conducted on trees, whereas the behavior of more dispersed canopies with much lower diurnal water storage than trees and with complex geometry that changes with time, as is the case with annual crops, remains poorly understood to date.

The P and L bands are more suitable for tree canopies because they allow penetrating the canopy and interacting with the trunk and branches and not only with the upper leaves (as is the case with C-band). Nevertheless, for short and less dense canopies with small components (compared to forests) such as wheat, the C-band is more adapted to extract information on vegetation while minimizing the contribution of the ground. Indeed, the complex combination of different scattering mechanisms from soil and vegetation at C-band makes it a valuable source of vegetation information (Ouaadi et al., 2023, 2020b; Van Emmerik et al., 2015), especially at high incidence angles. In this context, the objective of this paper is to investigate, for the first time, the intra-day variation of C-band temporal coherence of wheat over the agricultural season, and to physically interpret these variations in terms of soil and vegetation variables.

The paper is organized in four sections as follows. The next section presents the study area, the radar experiment and data processing. Section 3 is devoted to the results presentation and it is organized as follows. First, the diurnal cycle of 15-min temporal coherence and the seasonal time series of its daily average are analyzed using

meteorological, micro-meteorological and vegetation data for different sub-periods of wheat growth season. The impact of incidence on temporal coherence is also assessed for three ranges of incidence angles. Second, the impact of irrigation events and morning dew formation on temporal coherence with baselines from 15-min to 23-h is investigated. Third, the temporal coherence for baselines from 1 to n days ($n \in [11,22]$ depending on the sub-period of the season) is studied and compared to the 6-day baseline acquisitions of Sentinel-1. Section 4 and Section 5 are dedicated to results discussion and conclusions, respectively.

2. Study site and data description

2.1. Study site

The experiment is carried out within a wheat field located in a private farm in the Haouz plain in Morocco (Fig. 1). The climate in the region is semi-arid Mediterranean characterized by low average temperature values in winter (~5 °C in January) and high average values in the summer (~35 °C in August). The annual average rainfall is around 250 mm and the reference evapotranspiration is about 1600 mm (Jarlan et al., 2015). The cereals are the main crop cultivated in the plain where about 51% of the irrigated area (third of the total surface) is dedicated to cereal production (Abourida et al., 2008). The radar experimental setup is installed at the top of a tower of 20 m high targeting the wheat field of about 1.5 ha. The field was sowed with winter wheat on 25th January 2020 and harvested on the 6th June. After sowing, a system of drip irrigation is installed. Note that the soil roughness is considered constant throughout the season as no soil work was carried out after sowing.

2.2. Meteorological, eddy-covariance and complementary field data

The wheat field was monitored by numerous measurements throughout the agricultural season. These measurements consist of automatically acquired measurements by the meteorological and the eddy-covariance stations and others collected during measurement campaigns. The weather station (Campbell Scientific) is installed over an alfalfa field, next to the wheat field as illustrated in Fig. 1, and records half-hourly measurements of wind speed, air temperature, relative air humidity and precipitations. The eddy-covariance station is equipped with CSAT3-3D sonic anemometer to measure the wind speed components and a KH2O-Krypton hygrometer to measure the water vapor fluctuations. The measured data, sampled at 20 Hz, are then processed using the'ECpack' software (van Dijk et al., 2004) to estimate the latent heat flux or evapotranspiration (LE) with a 30 min time step. Near the eddy-covariance tower, a network of TDR probes is installed underground to estimate the soil moisture every 30 min at different depths, including the root zone soil moisture (RZSM) at 10, 20 and 30 cm depth in addition to the surface soil moisture (SSM) at 5 cm depth. For the latter, the measures of two sensors installed one under and the other between the drippers were averaged to obtain a representative measure of the field. Indeed, the drip irrigation system installed on the field is

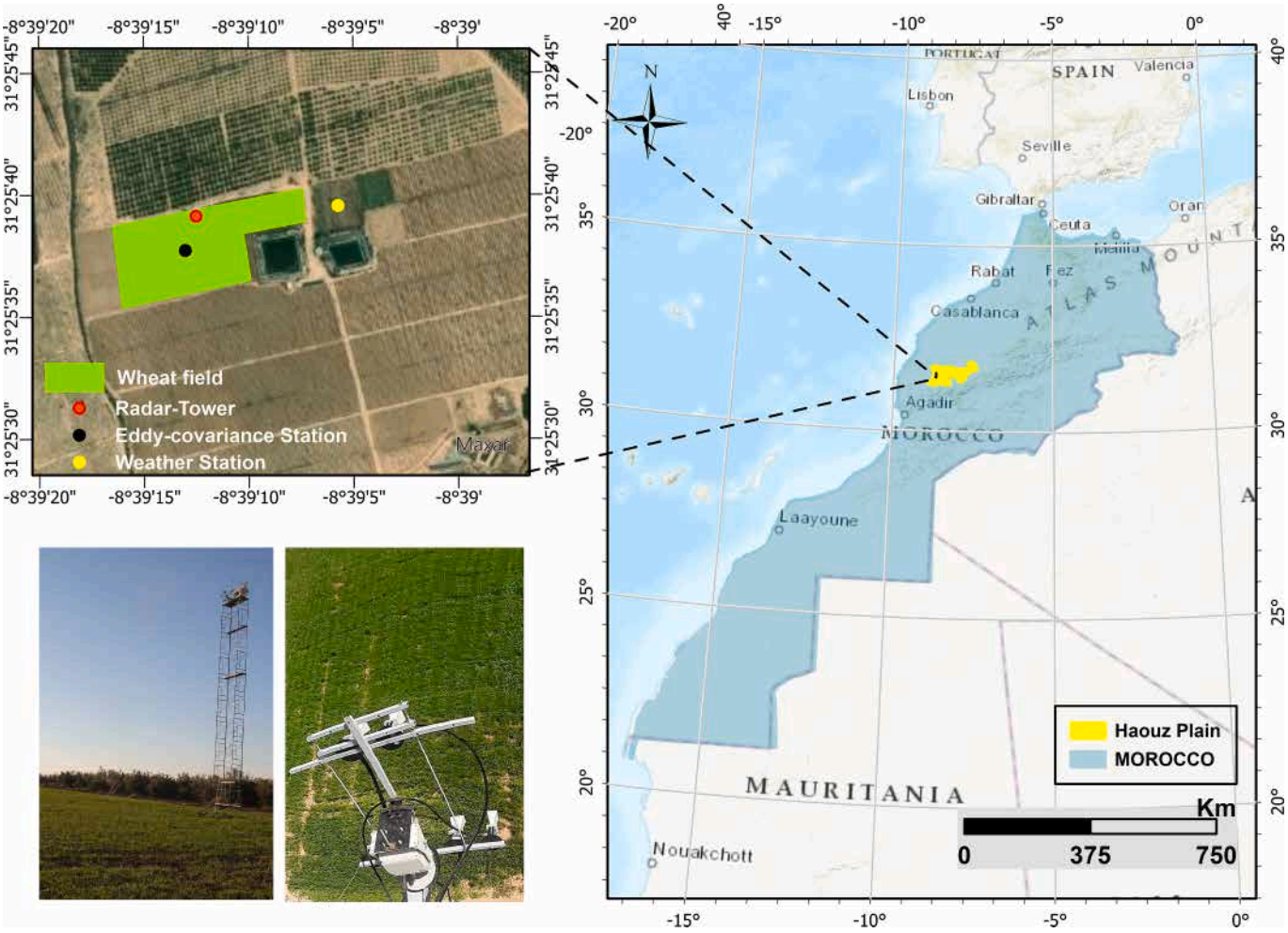

Fig. 1. Location of the wheat field in the Haouz plain in Morocco (right map). The location of the radar tower (illustrated by the two photos in the figure), eddy-covariance and weather stations are also indicated in the left map.

characterized by equally-spaced pipes (0.7 m) equipped in turn with equally-spaced drippers (0.4 m) ensuring a flow rate of 7.14 mm/h per dripper. This results in a homogeneous distribution of moisture across the field. The surface soil temperature (T_{soil}) is also measured at a 5 cm depth using TDR probes. Measurement campaigns were scheduled throughout the season every 15 days on average to measure vegetation water content and aboveground biomass. Destructive technique was adopted for this purpose; 8 samples are taken by quadrats of 25*25 cm^2 selected randomly over the field. Samples are first weighed in the field and then transported to the oven for drying. After 48 h in the oven at 105 °C, the samples are weighed again to calculate the aboveground biomass (AGB). The difference between before (field sample weight) and after oven drying is first computed and then divided by the field sample weight to obtain the vegetation water content (VWC) in percent. The canopy height was also measured by averaging ten measurements taken at random locations over the field.

Figure 2 provides an overview of the water status of the field including the wheat canopy and the underlying soil throughout the season. 7 sub-periods of the season that will be used in the results section are also reported in Fig. 2, including 5 phenological stages (tillering, extension, heading, maturity and senescence) of wheat defined from the field observations, a period in the beginning of the season when the soil is almost bare and a post-harvest period. The latter two sub-periods are considered to show the temporal coherence dynamic over wet and dry bare soil, respectively. Rainfall measurements show that the 2020 season was a dry season with only 70 mm recorded between sowing and harvest. This explains the regular irrigation of the field by the farmer. For the sake of information, irrigation timing and amounts are available up to March 15 when the COVID confinement has prevented data gathering. Subsequently, the irrigation dates are estimated from the SSM time series by considering the increase of SSM when no rain event was recorded. The amount after March 15 is set at the average value of previously recorded irrigation amounts. Available water (AW) represents the total amount of water in the root zone. It is calculated as follows from SSM and RZSM measurements at different depths (Rafi, 2020):

$$AW = \frac{(SSM - \theta_{wp})h_5 + \sum_{i=1}^{n}(RZSM_i - \theta_{wp})h_i}{(\theta_{fc} - \theta_{wp})\sum_{i=1}^{n} h_i} \quad (1)$$

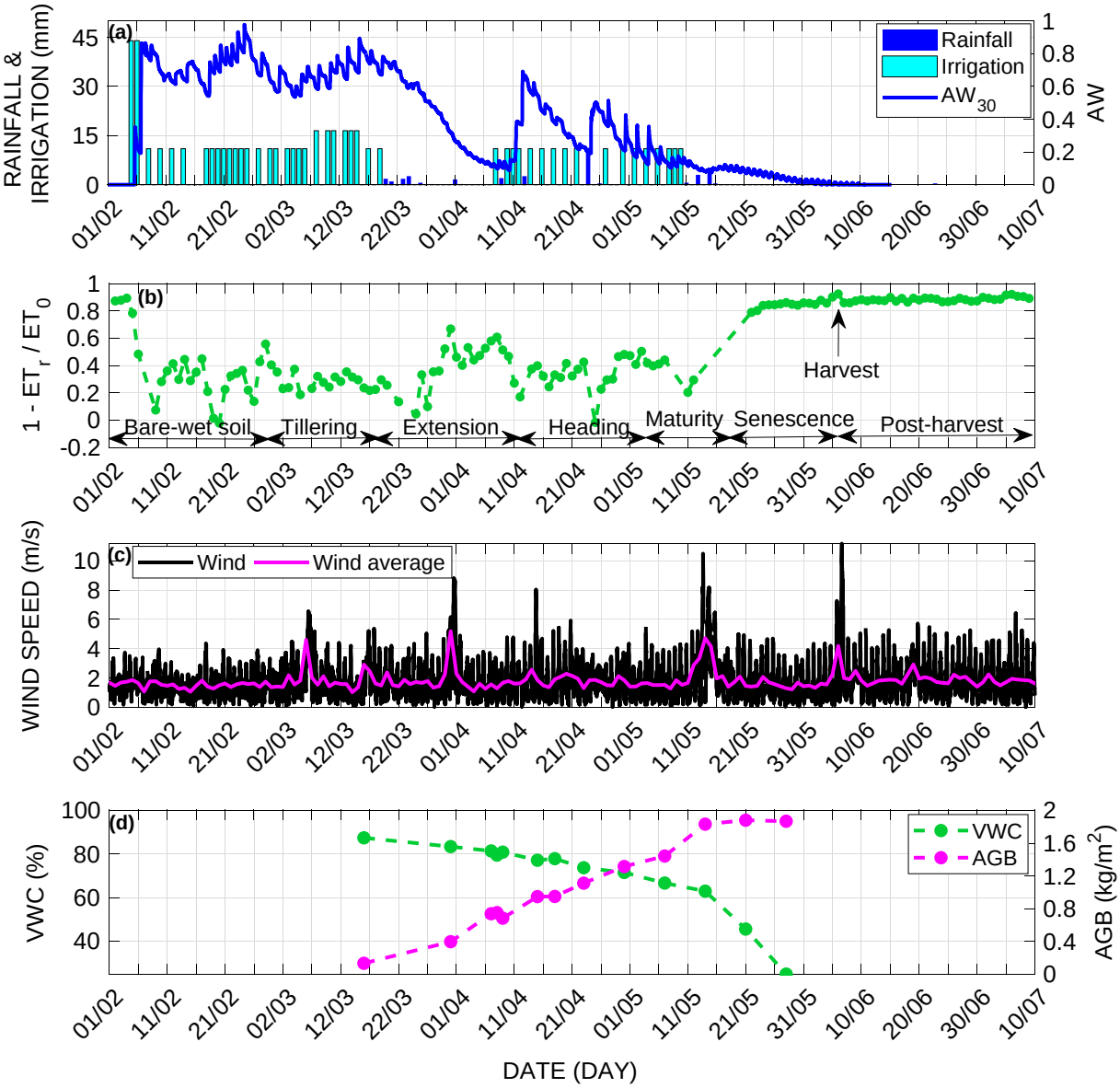

Fig. 2. Time series of the in situ variables including, rainfall, irrigation, AW_{30}, $1 - ET_r/ET_0$, wind speed, VWC and AGB over the wheat field during the 2020 season. Please note that irrigation dates and amounts were estimated from SSM measurements after March 15 (see text).

Where θ_{wp} and θ_{fc} are the soil moisture at the wilting point and the field capacity, respectively. $RZSM_i$ is RZSM at i depth and h_i is the soil layer thicknesses monitored by the corresponding sensor. Available water content for root is computed from the 0–30 cm soil moisture measurements. Indeed, Chen et al. (2021) have reported that the drip irrigation technique is limiting the rooting depth of wheat to the 0–20 cm layer. This depth can be increased up to 40 cm at most drier conditions (Chen et al., 2021; Plant et al., 1988). A triggered water stress was implemented in the field by stopping irrigation from March 20 to April 4 (Fig. 2a). It is characterized by a drastic drop of the available water in the soil as illustrated by AW_{30} (AW in the soil layer depth of 30 cm). To check the effect of this stress period on the vegetation, the index $1 - ET_r/ET_0$ is plotted in Fig. 2b. ET_r is obtained by cumulating daily values of LE and then converting to mm/day. ET_0 is the reference evapotranspiration that account the evaporating power of the atmosphere. It is computed from the meteorological forcing using the FAO-56 Penman-Monteith equation (Allen et al., 1998). $1 - ET_r/ET_0$ ranges from 0 ($ET_r = ET_0$; no stress) to 1 ($ET_r << ET_0$; fully stressed). The evolution of this index shows that its values are overall between 0.2 and 0.4 until March 20. The index drops to zero on certain days of the season, including around February 19, March 22, April 25 and May 11. This is mainly a consequence of ET_0 reduction due to cloudy-rainy periods associated with the low incoming solar radiation. By contrast, higher values between 0.4 and 0.6 were reached during the stressed period to recover the non-stress values after the new onset of irrigation around April 10. It is, however, important to point out here that the highest values achieved (0.6) indicate that the applied stress was moderate. After May 21, values around 0.8 are obtained as a result of increasing ET_0, a consequence of high climatic demand at the beginning of summer while irrigation is stopped. Indeed, ET_r is about 0.6 mm/day at this time of the season. Also, a significant drop (~20%) in VWC (Fig. 2d) is observed from about 60% on May 14 to about 40% on May 21. At this time, biomass has reached its maximum as illustrated by AGB that gradually increased during the season to peak at 1.9 kg/m^2 around May 21. The recorded wind speed values are between 0 (at night) and 4 m/s and the daily average is about 2 m/s. Nevertheless, some extreme strong wind values that can reach up to 10 m/s (Fig. 2c) were also recorded.

2.3. Satellite data

2.3.1. Sentinel-1 data

Sentinel-1 is an ESA's constellation composed of two C-band satellites A and B launched in 2014 and 2016, respectively, with a 6-day revisit time before the failure of Sentinel-1B on December 23, 2021. The study area is covered by two orbits 52 (Descending, overpass at 06 h36) and 118 (Ascending, overpass at 18 h41), observing the field at incidence angles of 35.2° and 45.6°, respectively. A total of 56 (28 per orbit) of SLC (Single Look Complex) products acquired in the Interferometric Wide-swath mode are downloaded for the period from February, 1 to July 10, 2020. The coherence is computed from the SLC products using SNAP application in five steps: i) "Apply-Orbit-file"; ii) "Back-geocoding"; ii) "Coherence"; iv) "TOPSAR-Deburst" and; v) "Terrain-Correction". The average of the pixel values within the field is computed and considered as representative of the field. For further details on the processing chain, the reader can refer to Frison et al. (2018) and Ouaadi et al. (2021).

2.3.2. Sentinel-2 data

Sentinel-2 is an ESA optical constellation comprising two satellites, A and B, with a revisit time of 5 days in cloud-free conditions. L-2 A products corrected from atmospheric effects are available free of charge from the THEIA website (https://theia.cnes.fr/). 20 cloud-free products have been downloaded for the monitored period (February 1 to July 10, 2020) and NDVI is computed and averaged over the field for each date.

2.4. Ground-based radar setup

2.4.1. Experiment description

The radar setup is composed of a Vector Network Analyzer (VNA) connected to the antennas through an electromechanical duplexer which is connected on the other side to a computer. The electromechanical duplexer has the task to switch between V- and H-polarized antennas by routing the signal between the VNA and the specific antenna pair. The radar system is composed of 6 horn C-band antennas: two are transmitters and four are receivers, forming thus eight pairs with 2 pairs per polarization (HH, HV, VH and VV). The pointing angle of the antenna is 40° below the horizon, with a 3 dB beamwidth of 55° and 50° for the E and H planes respectively (El Idrissi Essebtey et al., 2019), providing along-range swath from 11 m to 53 m (for 30° and 70° incidence), and along-azimuth swath from 20 m to 50 m (for 30° and 70° incidence). The antennas are installed over a mobile turret which enables 4 depointing angles of $\pm 10^{\circ}$ and $\pm 20^{\circ}$ around the center position; resulting in five azimuths from 160 to 200 (160, 170, 180, 190 and 200). A two-pair has been installed for each polarimetric channel for increasing the number of independent looks (Section 2.4.2). Besides, such antenna array design also provides interferometric capabilities, as well as backup redundancy in case of hardware failure.

The acquisitions are performed continuously with a time step of 15 min. Data are recorded on a hard disk and then transmitted to a server in a control room. The acquisition cover a frequency bandwidth $\Delta f = 0.6$ GHz (5.2–5.8 GHz) with $Nf = 1601$ points. The acquisition is an impulse response recorded as a complex number in the frequency domain with a frequency step $\partial f = \Delta f / Nf - 1 = 375$ KHz. This implies an unambiguous range $d = c/2\partial f = 400$ m and a range resolution $dr = c/2\Delta f = 25$ cm. To increase the number of looks, each acquisition for a given pair of antennas is repeated three times, resulting in three sequences (A, B and C).

2.4.2. Data processing

The data in the frequency domain are transformed into the time domain using a fast Fourier transform. An example of a resulting range impulse is illustrated in Fig. 3. The wheat field response starts almost at 20 m in range. To avoid edge effects and to select a relevant number of samples within a limited range of incidence angles, a range interval between $r_{min} = 28$ m and $r_{max} = 40$ m is considered (resulting in 48 range cells). This corresponds to a range of incidence angle of 45° - 60°. Considering 3 sequences, 48 range cells and 2 antenna pairs (by polarization), the resulting number of independent looks (< 3*48*2) can be estimated from the equivalent number of looks (ENL) following the method used in El Idrissi Essebtey et al. (2019). First the ratio between the coefficients of variation square from a single pair, single sequence and the two pairs, 3 sequences gives the ENL gain from pairs and sequences. The ratio is then multiplied by the number of range cells. As for the annual crops, the vegetation develops from sowing to harvest, the average value of the ratio is changing from a minimum of about 2.5 at the beginning of the season (and during the night hours) until a maximum of 6 in the full development of wheat around 17 h and 18 h when the wind reaches its highest values. This range of values results in a number of independent looks between 120 and 288 ensuring thus a negligible bias of temporal coherence higher than 0.2 and a bias lower than 0.1 for temporal coherence lower than 0.2.

The tower response is assumed to be constant throughout the season. However, changing environmental conditions (i.e. effect of temperature and rainfall on electronic devices) lead to temporal variations in the tower response between antennas. In order to account for these residual system temporal changes in spite of the VNA calibration sequence before each acquisition cycle, the coupling peak in the impulse responses (cf. Fig. 3) is used as in Hamadi et al. (2014) to constrain in amplitude and phase its values to reference ones. The temporal coherence ρ_{pq} at pq polarization is computed using the formula:

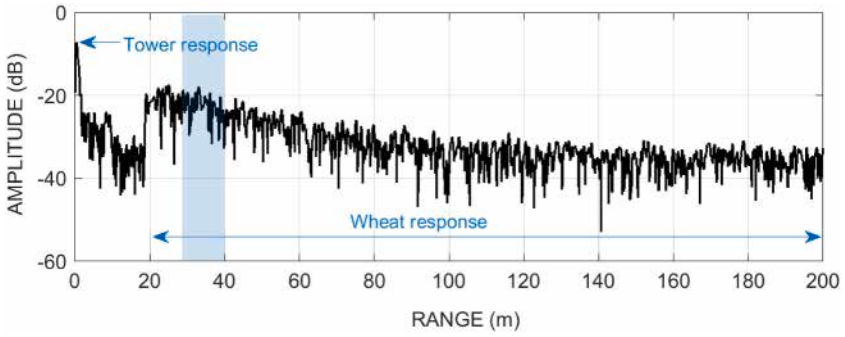

Fig. 3. Example of an impulse response over the wheat field for the entire range showing the tower and the wheat field responses. The blue shaded area corresponds to the range interval [28 m, 40 m] considered in this study. (For interpretation of the references to colour in this figure legend, the reader is referred to the web version of this article.)

$$\rho_{pq} = \frac{\left|\sum_{k=1}^{2}\sum_{s=A}^{\{A,B,C\}}\sum_{r=r_{min}}^{r_{max}} S_{pq,t_1}^{s,k}(r).S_{pq,t_2}^{s,k}(r)^{*}\right|}{\sqrt{\sum_{k=1}^{2}\sum_{s=A}^{\{A,B,C\}}\sum_{r=r_{min}}^{r_{max}}\left|S_{pq,t_1}^{s,k}(r)\right|^{2}.\sum_{k=1}^{2}\sum_{s=1}^{\{A,B,C\}}\sum_{r=r_{min}}^{r_{max}}\left|S_{pq,t_2}^{s,k}(r)\right|^{2}}} \quad (2)$$

Where $S_{pq,t_1}^{s,k}$ is the complex range-acquisition at range r at time t_i (i = 1, 2, the acquisition) of the k antenna pair and s sequence. The temporal coherence (hereafter called coherence to simplify) is computed between two acquisitions separated with a temporal baseline $t_2 - t_1$. From here on, the baseline will refer to $t_2 - t_1$ and reference date to t_1.

The imperfect isolation between cross-polarized and co-polarized channels in radar systems induces a disturbance (or overlap) between the signals leading to correlation between the channels (Al-Kahachi et al., 2014; Freeman et al., 1990). This electromagnetic phenomenon, known as crosstalk (Freeman et al., 1990), is even more important with the antenna proximity, and must be accounted for before fully polarimetric analysis, either based on external calibration targets (Van Zyl, 1990) or by the data itself and symmetry assumptions (Quegan, 1994). In this study, data from the VV polarization are used while the other polarizations are not presented as crosstalk correction is not yet applied. For the sake of information, broadly similar behavior was observed when using the other polarizations.

Because of electrical failures, support tour movements, interventions and work around the tower, data is not available for some days. Table 1 provides the number of days available for each sub-period. In particular, from the senescence period onward, a high number of outliers were recorded such as low coherence values lower than 0.2 during the night most likely because of the turret dysfunctioning that did not come back to the expected location. To overcome this dramatic lack of observations during this period, the data were filtered and corrected as follows: (i) values lower than 0.3 were first discarded as it was observed that during the days when the acquisition was made properly, the coherence never fell below 0.3; and (ii) the maximum of the coherence for the 5 azimuths was considered assuming that the field is homogeneous. Finally, a total of 7 days (over the total 18 days of the period duration) are considered for the senescence period among which 5 days were processed following the method described above. Likewise, 12 days are considered from a total of 33 days for the post-harvest sub-period using the same method. Please note that several tests have been performed with different range intervals (between 25 m and 70 m) but the same behavior was observed for the senescence and post-harvest sub-periods. For the 6 sub-periods before senescence, the coherence is computed from the 180 azimuth data but similar results were also obtained for the other azimuths giving the homogeneity of the wheat field.

3. Results

The time series of temporal coherence with a 15-min temporal baseline are first analyzed jointly with the meteorological, micrometeorological and vegetation data at both daily and seasonal scales for different sub-periods of the season. Then, the impact of irrigation and morning dew in temporal coherence with baselines from 15-min to 23-h is investigated. Finally, longer baselines are considered in order to provide insight for future repeat-pass spaceborne coherent radar missions in terms of revisit period and time of acquisition.

3.1. 15-min temporal coherence diurnal cycle and seasonal course

3.1.1. Temporal coherence diurnal cycle

Figure 4 shows the daily cycles of the hourly values of coherence with a 15-min temporal baseline (obtained by averaging the four 15-min baseline values per hour) at VV polarization (ρ_{VV}), of evapotranspiration, SSM and wind speed for the 7 sub-periods identified above. Diurnal cycles are represented by boxplots: the median value is indicated in red while box bottom edge indicates the 25th percentiles and box top edge shows the 75thpercentiles.

For the bare soil periods at the start of the season or after harvest, ρ_{VV} values remained stable around 1 along the day as expected. By contrast, as soon as the wheat started to grow and to cover the soil, a decorrelation is observed during daytime exhibiting a clear diurnal cycle whose amplitude increased with the canopy development. Indeed, the amplitude was increased by 85% from tillering (minimum ρ_{VV} around 0.9) where the soil contribution still significant to maturity (minimum ρ_{VV} around 0.3). This was followed by an amplitude reduction of 64% from maturity to senescence as the vegetation dries out. Coherence values are stable and high around 1 during the night. At this time, wind speed is low ($\sim$ 1 m/s) and the vegetation is at rest (LE $\sim$ 0 W/m^2). At dawn, between 06 h and 08 h depending on the sunrise time, coherence starts to decrease until the end of the afternoon (gray shaded areas in Fig. 4). A first striking result already highlighted by previous similar studies carried out on forests is the concomitance between the strongest decorrelation in the late afternoon and the daily maximum of wind speed values. Indeed, the minimum daily coherence is significantly correlated to the maximum daily wind speed with a correlation coefficient r = 0.7 (significant at the 99% level following the student's t-test). In addition, this late afternoon decorrelation increases from tillering to maturity with

Table 1
Number of days with radar data available for the different sub-periods of the 2020 season.

	Bare-wet soil	Tillering	Extension	Heading	Maturity	Senescence	Post-harvest
Number of days with available data	14	19	20	14	9	7	12

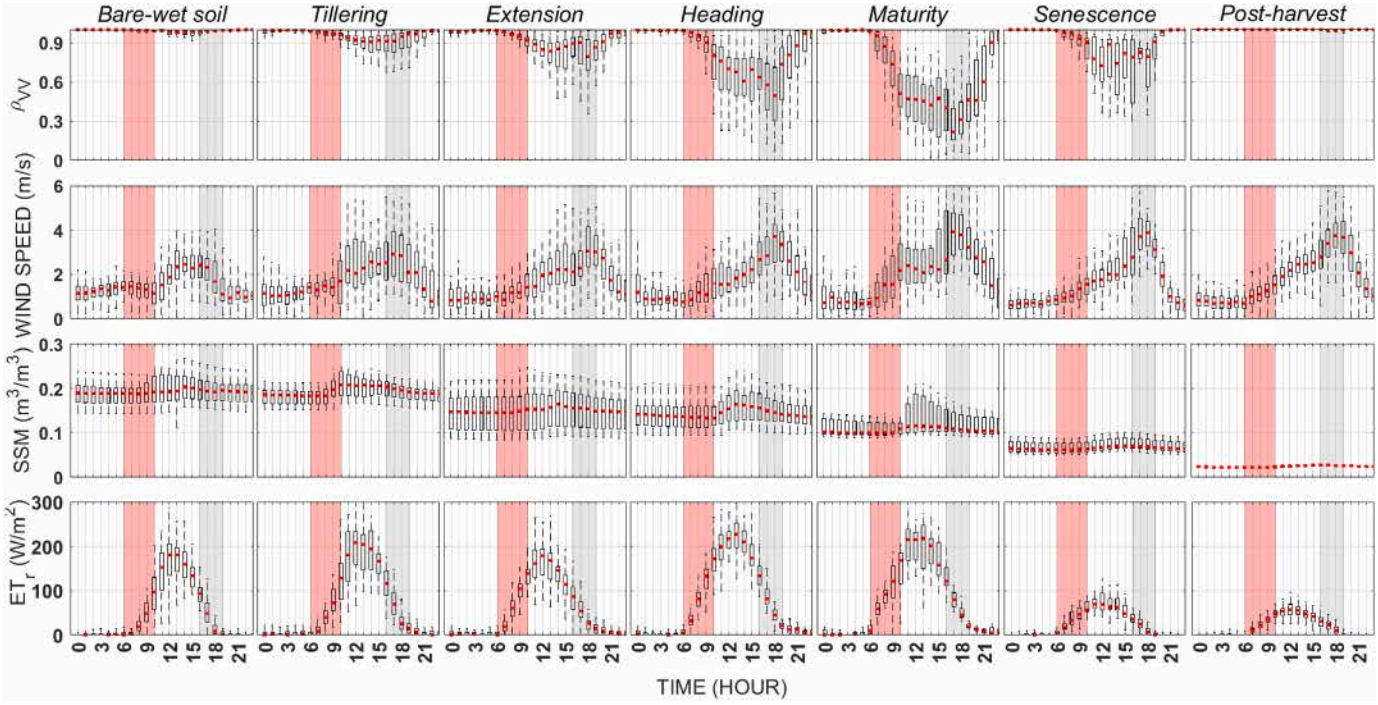

Fig. 4. Diurnal cycles represented by boxplots (median is indicated in red, the box bottom edge indicate the 25th percentiles and the box top edge show the 75th percentiles) of ρ_{VV} with 15-min baseline, wind speed, SSM and LE for 7 different sub-periods of the wheat season (see text). The morning decrease and evening increase of ρ_{VV} are shaded in red and gray, respectively. (For interpretation of the references to colour in this figure legend, the reader is referred to the web version of this article.)

above-ground biomass. After 18 h, ρ_{VV} increases as the wind speed decreases. ρ_{VV} finally recovers its highest values between 21 h and 23 h depending on the period.

The morning drop, during 2 to 3 h after dawn (red shaded areas in Fig. 4), cannot be explained by the wind-induced motion of the scatterers as wind speed values remain low at this time. In order to go further into the analysis, days with wind speed in the morning (<1.6 m/s) while wheat is fully covering the soil (total of 8 days) were isolated. The relationship between ρ_{VV} and wind speed with a 15-min time step were analyzed during morning and night hours (cf. Fig. S3 in the supplementary material). The results show that ρ_{VV} in the morning displays a decreasing trend compared to the night when vegetation is at rest. In particular, for wind speed lower than 1 m/s, 99% of the data exhibit ρ_{VV} values above 0.97 during night period (00 h15 to 01 h30) while only 69% of values are above this threshold during the morning period (07 h15 to 08 h30). At dawn, the plant starts the photosynthetic process and the associated water uptake by the roots in response to increasing incoming solar radiation. This water movement within the plant xylems probably causes a displacement of the phase center explaining the observed coherence drop. Unfortunately, no sapflow measurements quantifying the real water uptake by the plant (i.e. the transpiration flux) were available during the experiment. Nevertheless, while evapotranspiration cannot be considered as a pure proxy of vegetation functioning as it includes the evaporation flux that can be strong just after a rain or irrigation event when the canopy is sparse, evapotranspiration is largely dominated by transpiration (around 80%; (Aouade et al., 2016)) when wheat is fully covering the ground (from mid-March in this study). Furthermore, evaporation should be very limited in this study as the irrigation is ensured using the drip technique and the recorded rainfall events are rare with very low amounts (c.f Section 2.2). To highlight the potential effect of the plant physiological processes on coherence morning drop, the correlation between the rate of LE increase and the coherence drop intensity is computed. To this objective, only clear-sky days are considered in order to withdraw days with low incoming radiation that are associated with reduced photosynthetic activity. To do so, days with incoming solar radiation showing a clean parabolic shape are selected by visual inspection considering the period from mid-March to beginning of the maturity stage when wheat is fully covering the ground and photosynthetically active. The morning period extends from dawn estimated when solar radiation is above 5 W/m^2 to dawn plus 3 h and a simple linear regression is computed on LE and on coherence. A high correlation of $r = 0.8$ (significant at the 99% level) between the morning slopes of ρ_{VV} and LE is observed, highlighting a striking sensitivity of coherence to physiological processes. This sensitivity can be shown during the early morning hours thanks to low wind speed values.

Interestingly enough, SSM also exhibits a small diurnal cycle apart from the post-harvest period. It is characterized a maximum around 11 h probably because the farmer always schedule the irrigation at the same time of the day. By contrast, no capillarity rise can be observed in the early morning. The temporal coherence does not seem to be impacted neither during the wet bare soil period nor during the vegetative stage. Considering that the temperature theoretically impacts the soil dielectric constant, Fig. S4a in the supplementary material displays the diurnal cycle of soil temperature (T_{soil}) and moisture superimposed with ρ_{VV} considering a 15-min baseline. A close look on the diurnal cycles from February 19 to 25 while soil is almost bare at this time indicates that both increases of SSM and T_{soil} are rather synchronized with ρ_{VV} and poorly informative about their individual impacts. By contrast, the much stepper decrease of temperature lasting until dawn does not prevent from the recovery of high ρ_{VV} values much earlier during the evening. Hence, this is a confirmation that SSM could be the primary factor behind the diurnal variation of the C-band decorrelation during this vegetative stage. It is however possible that this small daily cycle could also be attributed to the low vegetation cover as the low diurnal cycle of SSM on February 17 is associated to marked daily cycle of temporal coherence. In addition, a finer time series analysis comparing days with irrigation and days without did not highlight any significant difference (not shown). However, it is probable that the reason is related to the drip irrigation technique used in this field that strongly limits the fraction of

wet soil with regards to sprinkler or flooding techniques.

3.1.2. Incidence angle impact

While the impact of incidence angle on the backscattering coefficient is well understood, angular signature of temporal coherence remains to be analyzed. Fig. 5 displays the diurnal cycle of temporal coherence at different sub-periods of the season for the following three ranges: [22, 28] meters, [28, 34] meters and [34, 40] meters, corresponding to 27° - 45°, 45° - 55° and 55° - 60° incidences, respectively. The three ranges are chosen so that the ENL is equal for all three. Considering 3 sequences, 48 range cells and 2 antenna pairs, the resulting number of independent looks is ranging between 48 and 72 during the agricultural season. These values are too low to guarantee a negligible bias on temporal coherence. Fig. 5 shows that, like for the backscattering coefficient, the higher incidence angle, the lower the temporal coherence. Indeed, the stronger contribution of the vegetation canopy leads to stronger decorrelation. In addition, this high decorrelation is more pronounced when vegetation is fully developed with temporal coherence values ranging from 0.6 for the range 27° - 45° to 0.3 for the range 55° - 60° during the late afternoon when wind velocity is the stronger. This corresponds to drop of decorrelation at 55° - 60° of 6% to 53% stronger than that at 27° - 45° from tillering to maturity.

3.1.3. Time series at the seasonal scale

Figure 6 shows the evolution of the daily median of 15-min coherence between 06 h and 20 h (night measurements are excluded as the plant is at rest and the wind is very weak and stable) at VV polarization over the season. The daily ET_r, wind speed, SSM, canopy height and Sentinel-2 NDVI are also displayed.

The $\rho_{VV-median}$ time series illustrates a seasonal evolution with four main periods (i) very high values, around 1, at the beginning of the season when soil is almost bare followed by (ii) a regular decrease progressively with the development of vegetation from tillering; (iii) an increasing trend is observed from the end of the maturity period; and (iv) $\rho_{VV-median}$ recovers finally its highest values after the harvest.

At the early start of the season, the soil is bare and there is no change of roughness as the soil was already worked out. $\rho_{VV-median}$ values maintained, as expected, around 1 which is a typical behavior of coherent scattering from stable component (Frison et al., 2018; Moeremans and Dautrebande, 2000; Ouaadi et al., 2020b). Afterwards, the $\rho_{VV-median}$ decrease is related to a combined effect of an increasing wind-induced movement of the scatterers and to the displacement of the phase center in response to the transpiration processes as already described above. In phase with $\rho_{VV-median}$, ET_r peaks at heading stage corresponding to grain filling. The minimum of $\rho_{VV-median}$ is reached in the maturity stage around May 9, 19 days after the canopy height peak

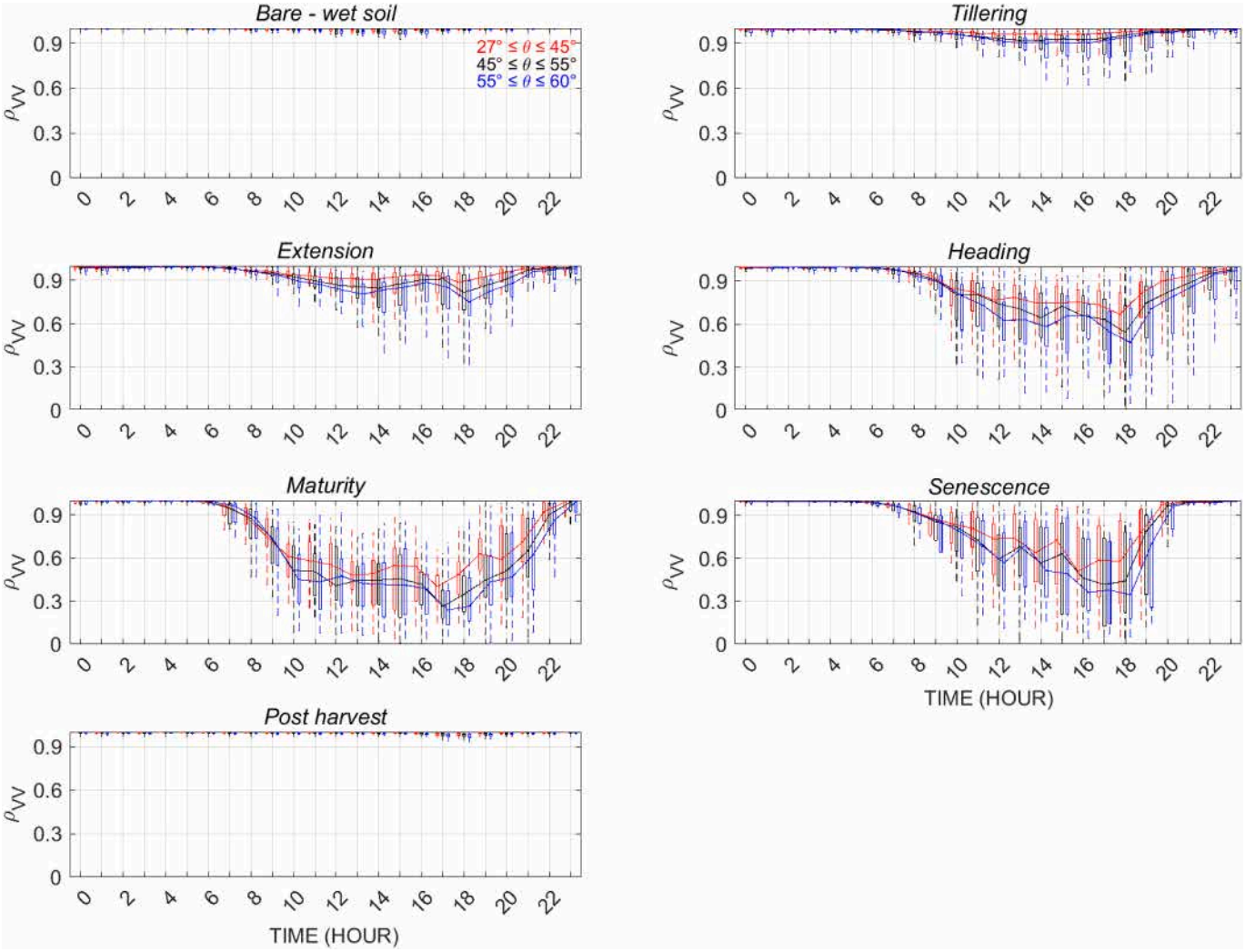

Fig. 5. Diurnal cycles represented by boxplots (median is indicated in red, the box bottom edge indicate the 25th percentiles and the box top edge show the 75th percentiles) of ρ_{VV} with 15-min baseline for three incidence ranges for 7 different sub-periods of the wheat season (see text). Continuous lines are connecting the medians for each incidence range. (For interpretation of the references to colour in this figure legend, the reader is referred to the web version of this article.)

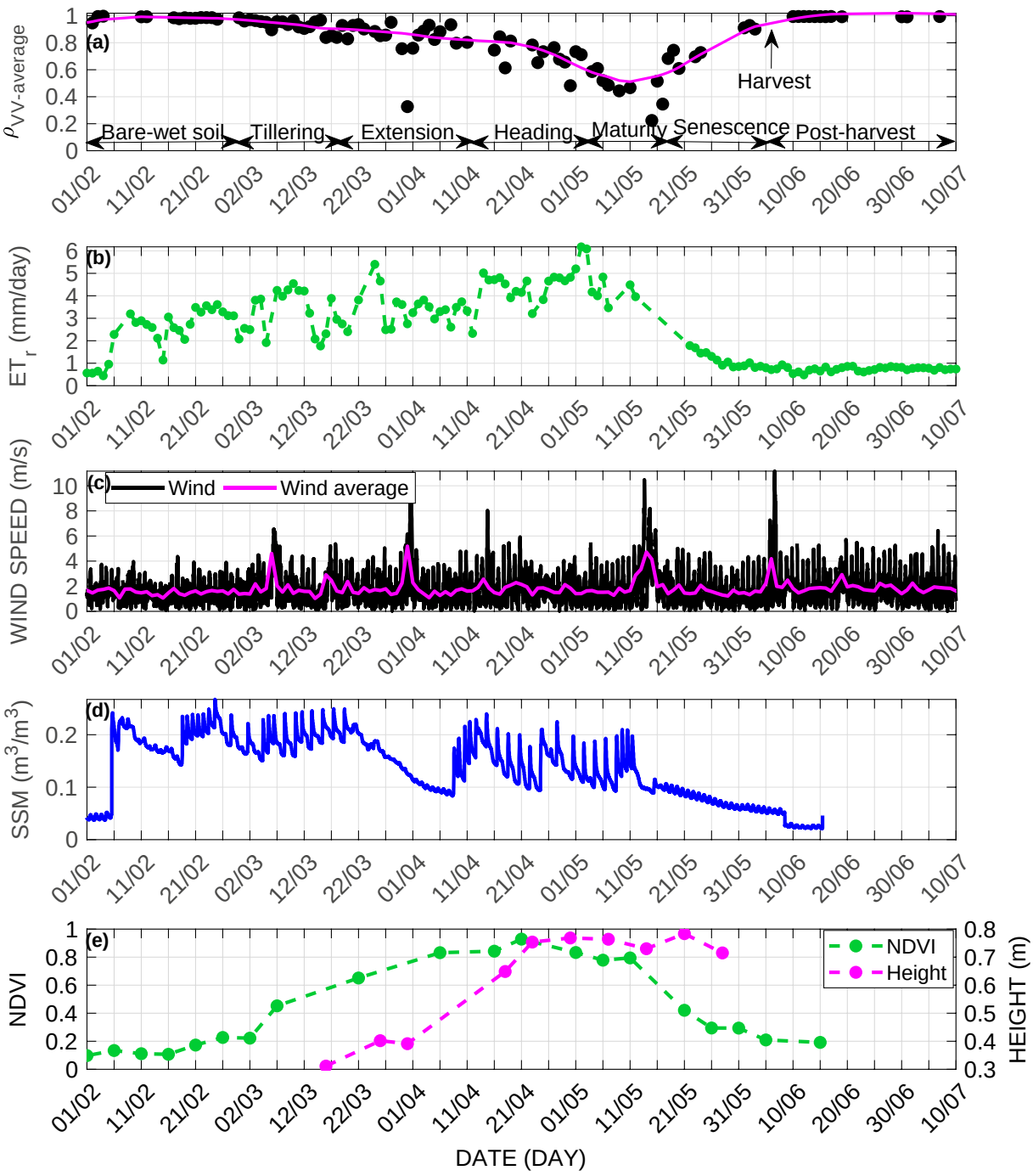

Fig. 6. Time series of (a) daily median of temporal coherence between 06 h and 20 h at VV polarization (The black dots are the observations and the magenta line shows the data smoothed using "rloess" method with a span of 20%), (b) daily ET_r, (c) half-hourly wind speed and daily averaged wind speed, (d) half-hourly SSM and (e) Measured canopy height and Sentinel-2 NDVI over the wheat field during the 2020 season. The sub-periods are also indicated in (a). (For interpretation of the references to colour in this figure legend, the reader is referred to the web version of this article.)

(April 21, Fig. 2e). This highlights the important contribution of leaves and heads size and orientation to the signal decorrelation. The increase in $\rho_{VV-median}$ from the end of the maturity is accompanied by a decrease in ET_r, indicating thus a decline in physiological functioning and water flow intensity through the plants. Indeed, plant is drying out at this time as illustrated by the drop of VWC and maximum of AGB (Fig. 2d) and by the NDVI decrease (Fig. 6e) from 0.8 on May 11 to 0.4 on May 21; the canopy gradually becomes transparent to the C-band signal. Interesting enough, a correlation of $r = 0.69$ (significant at the 99% level) is obtained between NDVI and and $\rho_{VV-median}$, supporting the potential of temporal coherence to monitor wheat development throughout the agricultural season already highlighted by previous studies using Sentinel-1 data (see for instance Barbouchi et al. (2022), Nasirzadehdizaji et al. (2021), Ouaadi et al. (2020b) and Villarroya-Carpio et al. (2022) among others).

SSM variation (Fig. 6d) shows a limited impact on $\rho_{VV-median}$ over the season. In particular, the triggered stress in late March/early April is barely visible neither on the time series nor on the daily cycle analyzed in the previous section (Fig. 4). During the period with the lower available soil water content (from March, 31 to April 7; cf. Fig. 2 and Fig. 6d), there was a violent windstorm that lasted between March 31 and April 2 (Fig. 6c) and the period corresponded to a strong growing

stage with ABG of the wheat that almost doubled. These specific conditions made difficult to disentangle the different factors and potentially highlight the effect of the triggered stress on the temporal coherence, in particular that the stress was moderate (cf. Section 2.2). Finally, a clear impact of strong winds can be observed with lower values of coherence corresponding to period of strong winds (around April 1 as already commented but also on March 6 and May 16); the intensity of the wind effect on $\rho_{VV-median}$ being obviously related to the density of the vegetation. For example, the effect of March 6 wind peak exists but it is much smaller than on April 1.

3.2. Temporal coherence with 15-min to 23-h baselines

3.2.1. Diurnal cycle

Figure. 7 shows the diurnal cycle of temporal coherence computed with a reference time at midnight and baselines range from 15-min to 23-h. To avoid repetition, only the main difference with the 15-min temporal coherence in Fig. 4 will be described here. Results show that coherence with baselines from 15-min to 23-h exhibits a strong decorrelation, apart from the bare soil periods as, by contrast with the 15-min baseline, they did not recover the high nighttime values. The decorrelation increased with the development of vegetation. Indeed, the minimum decreases from 0.5 (median) during tillering to 0.1 during the maturity stage. In addition, while the slope of the [00 h, 08 h] interval is similar between the early stage (tillering) and the late stages of growth (heading and maturity), it is much higher during the extension period. At this stage, the leaves are light, the canopy is scarce and therefore may be more sensitive to low wind speed than the later period, while at tillering there may still be a significant coherent contribution from the soil. After extension, the head layer makes the scatterers heavier and not easily displaced by the low winds recorded during the night. Interestingly enough, for extension, heading and maturity, there is no increase in coherence during the late afternoon as observed on the 15-min baseline daily cycle in response to the decrease of wind speed and a reduce incoming solar radiation limiting photosynthesis activity. By contrast, ρ_{VV} increases from a minimum of 0.2/0.5 at 18 h/20 h to 0.4/0.6 at 23 h for senescence/tillering. Our assumption here is that the coherent contribution from the soil causes this coherence gain. Finally, a small diurnal cycle is observed for bare-wet soil: decorrelation from 07 h reaching a median value ~0.85 at 15 h, and then increases but without recovering the initial value. Likewise, the dry soil after the harvest undergoes a daily evolution with a variation amplitude limited to 0.05 (observed between 13 h and 18 h) and it recovers its highest values hereafter. This could be related to sensitivity of ρ_{VV} (i) to small vegetation movements under limited wind speed and/or (ii) to the diurnal cycle of soil moisture. Note that the impact of T_{soil} on ρ_{VV} computed for baselines from 15-min to 23-h has also been checked for an almost-bare period of the agricultural season (Fig. S4b). Similar conclusions can be drown as for ρ_{VV} with a 15-min baseline (Fig. S4a, Section 3.1.1) but with a reduced diurnal cycle of ρ_{VV} with a 15-min baseline compared to ρ_{VV} with baselines from 15-min to 23-h.

3.2.2. Impact of irrigation and morning dew on temporal coherence

By contrast with the 15-min coherence, a possible effect of irrigation on ρ_{VV} calculated with baselines from 15-min to 23-h was observed. Fig. 8 shows the time series of ρ_{VV}, SSM and wind speed for two periods: (1) almost bare wet soil conditions (NDVI~0.2; cf. picture of the field taken on 02/28/2020 in Fig. S1 in the supplementary material) and (2) a period where the soil is moderately covered by vegetation (NDVI~0.6). The vertical dotted lines correspond to the start of the irrigation event. For information, no rain event is recorded during the two periods. For bare soil (Fig. 8a), a drop of ρ_{VV} is concomitant with the increase in SSM

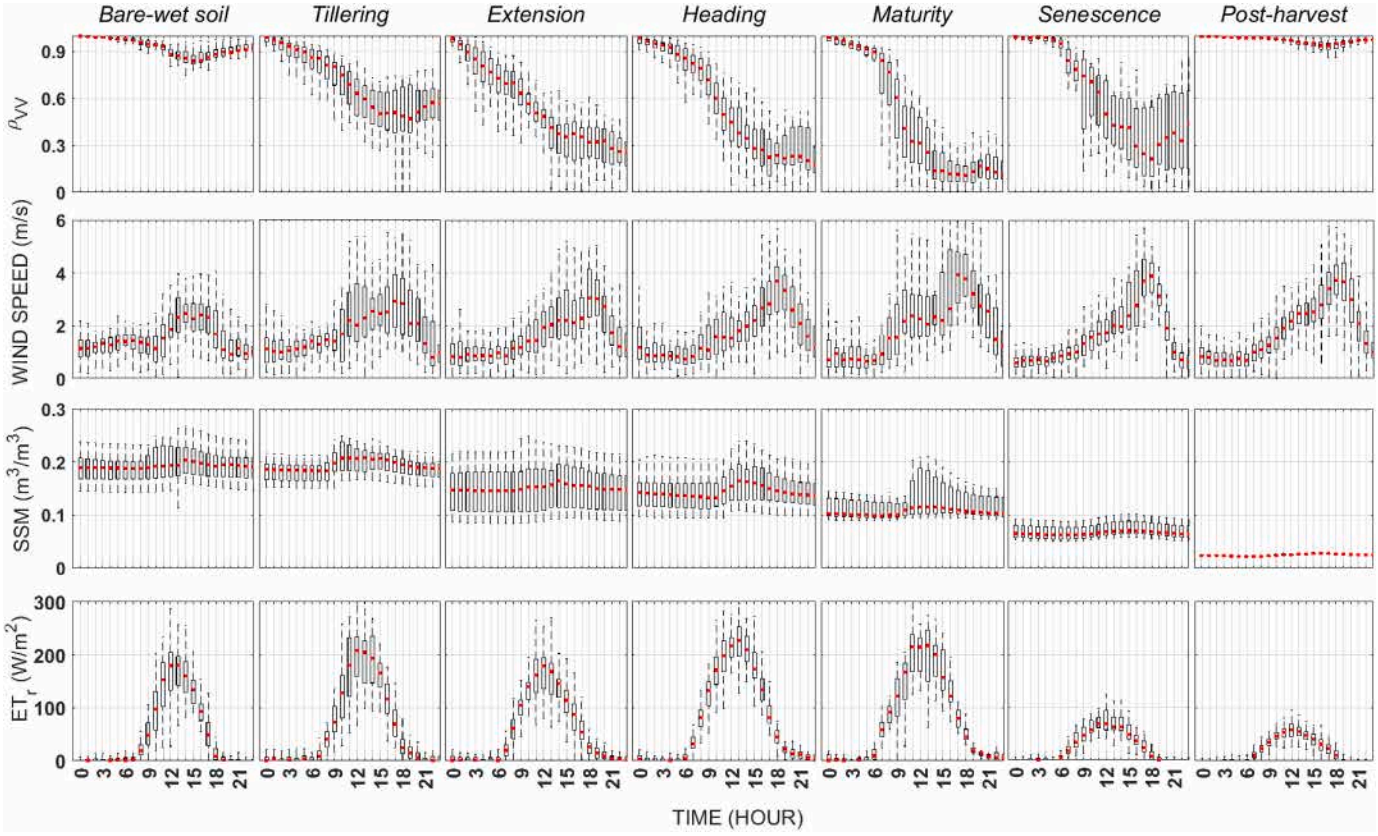

Fig. 7. Diurnal cycles represented by boxplots (median is indicated in red, the box bottom edge indicate the 25th percentiles and the box top edge show the 75th percentiles) of ρ_{VV} computed with baselines from 15-min to 23-h, of wind speed, SSM and LE for the 7 sub-periods (see text). (For interpretation of the references to colour in this figure legend, the reader is referred to the web version of this article.)

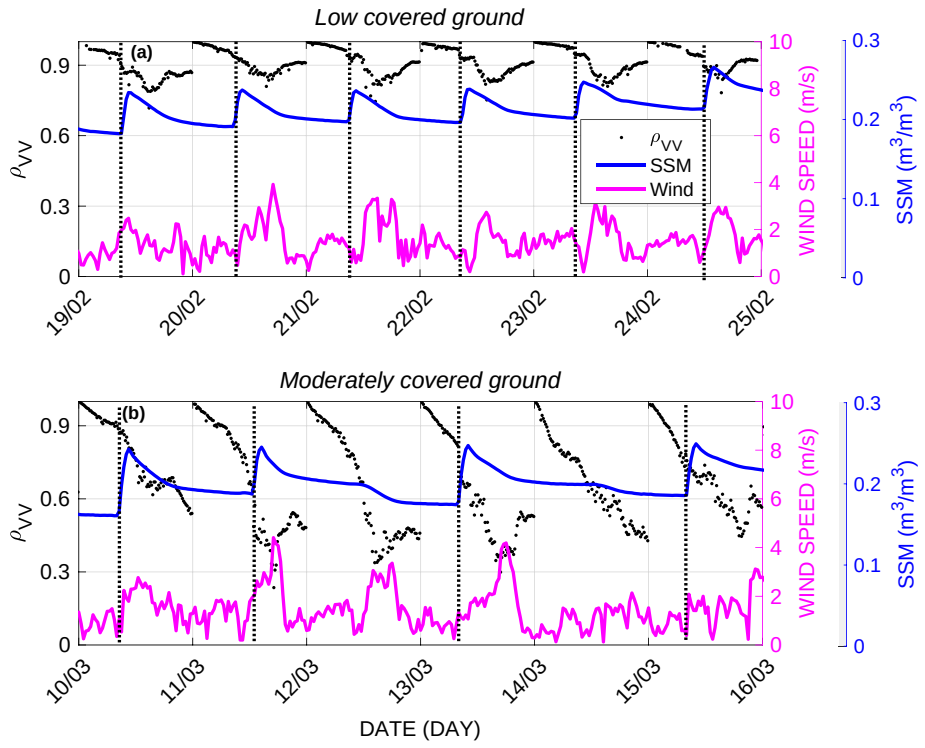

Fig. 8. Time series of temporal coherence computed for baselines from 15-min to 23-h over two periods: (a) almost bare soil and (b) moderately covered soil. Half hourly SSM and wind speed are superimposed. The vertical dotted lines indicate the SSM increase in response to irrigation.

associated with the start of the irrigation event for almost all days except on 20/02/2020. This decorrelation is probably due to a change of SSM driven by the application of irrigation as wind speed is low at this time apart from 19/02/2020. Nevertheless, the drop remains low, probably because of the limited area of wetted soil related to the drip irrigation technique. This coherence drop lasts shorter than the duration of the irrigation event and it is quickly followed by a period when there is no decorrelation anymore. Later in the season, as the canopy covers the ground (Fig. 8b), the abrupt decrease in ρ_{VV} at the start of the irrigation events is not observed anymore (true for the rest of the season) and ρ_{VV} slope change seems to be mainly governed by the dynamic of the wind speed.

Likewise, a fine analysis of the time series pointed out, for some days, an increasing trend of ρ_{VV} during a short period of time in the early morning hours usually between 07 h and 08 h both during days with and without irrigation. Therefore, the potential impact of morning dew formation was investigated by computing the dew point temperature (T_{dew}) from air temperature (T_a) and relative air humidity (RH) as follows (Lawrence, 2005):

$$T_{dew} = T_a - \frac{100 - RH}{5} \quad (3)$$

Where T_{dew} and T_a are in °C and RH in %.

Figure 9 shows the time series of ρ_{VV}, T_{dew} and T_a in the first subplot and SSM and wind speed in the second subplot for two periods: one with morning dew (Fig. 9a) and one without dew (Fig. 9b). The periods when T_a=T_{dew} are shaded in orange. There is a clear concomitancy between dew time and an increase of ρ_{VV} in the early morning. This increasing trend that can last up to 2 h is then followed by the initial decrease trend observed before dew formation. Given the semi-arid Mediterranean climate of the region, the presence of dew is not very frequent and it disappears quickly as the temperature increases due to high solar radiation. The effect of dew on the temporal coherence could be related to (i) a direct effect of the presence of liquid water at the leaf surface and/or (ii) a reduction of transpiration due to saturated air (cf. discussion section). During 2020 season, the number of rainfall events was limited, which hampered the investigation of its effect on ρ_{VV}. Nevertheless, the ρ_{VV} increase of the same order of value than for dew occurring at the end of the day on March 23 is concomitant with a rainfall event.

3.3. Temporal coherence with baselines above 1-day

3.3.1. Decorrelation analysis by sub-periods

In this section, the objective is to investigate the temporal evolution of coherence for a temporal baseline ranging from 1 to n days, depending on the sub-period of the season, in order to provide insight for future repeat-pass spaceborne coherent radar missions in terms of revisit period and time of acquisition. Sub-daily baselines are also added for comparison purposes (0.25 day corresponding to 6 h). The study is conducted on 6 sub-periods along the agricultural season already identified. The post-harvest period is not shown as it showed broadly similar dynamics as the bare-wet soil period. The results are presented in Fig. 10 using boxplots for a 06 h (6:00 a.m.) acquisition time at VV polarization. Fig. S2 in the supplementary material is the same as Fig. 10 but with a reference time at 18 h.

The lower decorrelation is obviously obtained during the wet bare soil period with ρ_{VV} remaining above 0.8 for baselines up to 4 days and above 0.4 up to 16 days. During tillering, the decorrelation increases and ρ_{VV} is below 0.4 after 9 days but remains close to 0.35 up to 14 days, thanks to a limited vegetation cover at this early stage of wheat growth. For the next vegetative stages, extension to maturity, lower and lower values of coherence are observed as the wheat develops with values slightly above 0.2 for extension after 1 day and < 0.2 for heading and maturity with the same baseline. The decorrelation seems less strong for senescence in response to vegetation drying. Considering the entire season, ρ_{VV} is around 0.3 after 1 day and drop to 0.1 for a baseline of 10 days. This indicates a strong decorrelation caused by the development of wheat and the change of the canopy structure throughout the season. Interestingly enough, the temporal coherence whatever the baseline is higher at 18 h than at 06 h for bare soil with values remaining above 0.6

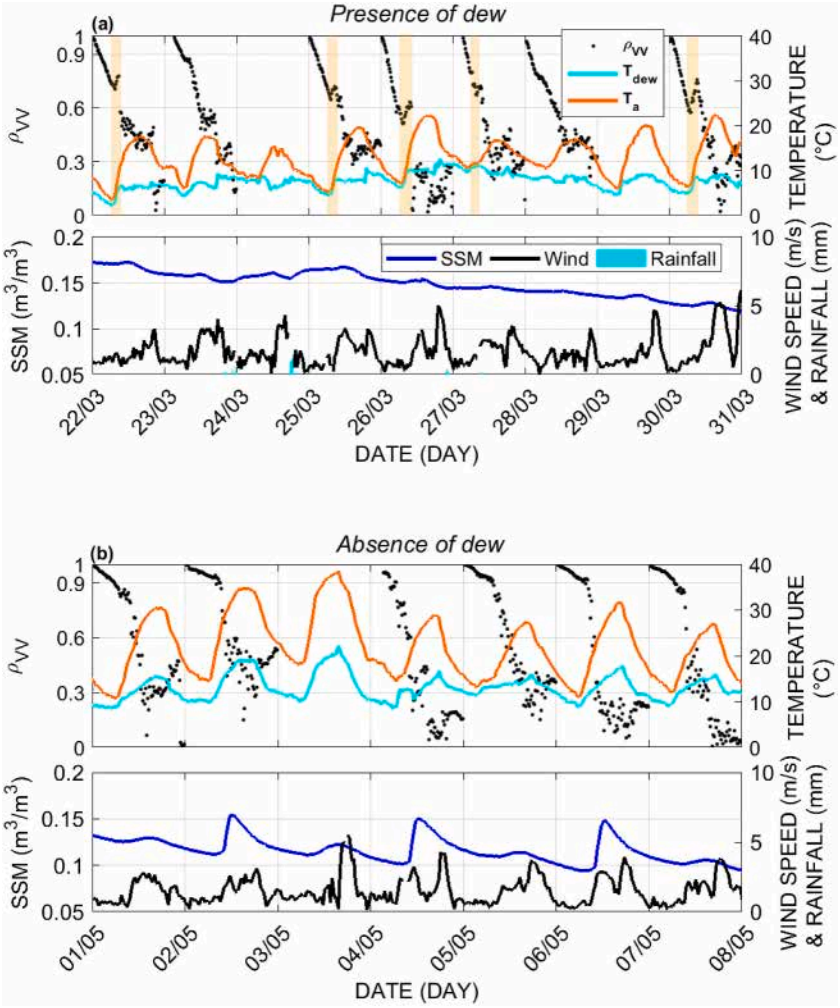

Fig. 9. Time series of ρ_{VV} computed for baselines from 15-min to 23-h over two periods: (a) during the presence of morning dew and (b) during the absence of dew. Air temperature and dew point temperature are plotted in the upper subplot for each period and the wind speed and SSM are plotted in the bottom subplot for each period. The shaded orange areas in (a) highlight the period of dew formation (T_a=T_{dew}).

up to 14 days. In contrast, and because of higher wind at this time, temporal coherence at 18 h is always lower than at 06 h from tillering to senescence.

3.3.2. *Comparison with 6-day Sentinel-1 acquisitions*

In order to compare with existing radar missions, typically Sentinel-1 which provides data free of charge, ground-based temporal coherence with a 6-day baseline is computed at the time of Sentinel-1 overpass considering ascending and descending orbits during the 2020 season (Fig. 11). Both signals are exhibiting a consistent seasonal cycle although the systems have some significant differences in terms of design and acquisition geometry. Indeed, both show high values at the start of the season, start to decrease progressively with the development of the canopy until Extension and recover progressively high values during crop senescence. The ground experiment exhibits higher amplitude of variation than Sentinel-1. The latter varies between 0.8 when the ground is bare, a slightly lower value than the ground-based measurement, and 0.2 when vegetation is fully developed. At this time, the ground experiment reaches values as low as 0.1. Similar values have also been reported at C-band over fully developed wheat (Nasirzadehdizaji et al., 2021) and over tropical forests (El Idrissi Essebtey et al., 2019). Comparison of the two Sentinel-1 orbits shows close values at both 35.2° and 45.6° incidence. Please note that restricting the incidence range of the ground based measurements in order to compare with Sentinel-1 is not possible as the number of looks would be too low (the range selection is explained at Section 2.4.2).

4. Discussion

The 15-min coherence exhibited a diurnal cycle whose amplitude depended on the phenological stage of wheat. The morning decrease of the diurnal cycle was found to be strongly correlated with the increase of evapotranspiration with a correlation coefficient of 0.8. This is in agreement with the previous studies (Albinet et al., 2016; Hamadi et al., 2014) carried out on tropical forest, including El Idrissi Essebtey et al. (2019) that highlighted a concomitancy of ET_0 daily onset with temporal coherence drop in the early morning. By considering actual evapotranspiration instead of ET_0 that reflects atmospheric demand only and not the actual water used by the plant, this study goes a little bit further as evapotranspiration is largely dominated by the transpiration flux related to the root water uptake and the physiological functioning of the plant when wheat plants are covering the ground as already highlighted. These studies are, however, novel and essential for understanding the behavior of temporal coherence, yet their results need to be extended in the future by further experiments covering other growth seasons together with the use of physical models. This is particularly relevant to properly disentangle the effect of plant physiology from the effect of wind.

Wind speed can also impact plant transpiration through the evaporative demand. Nevertheless, evaporative demand is mainly governed

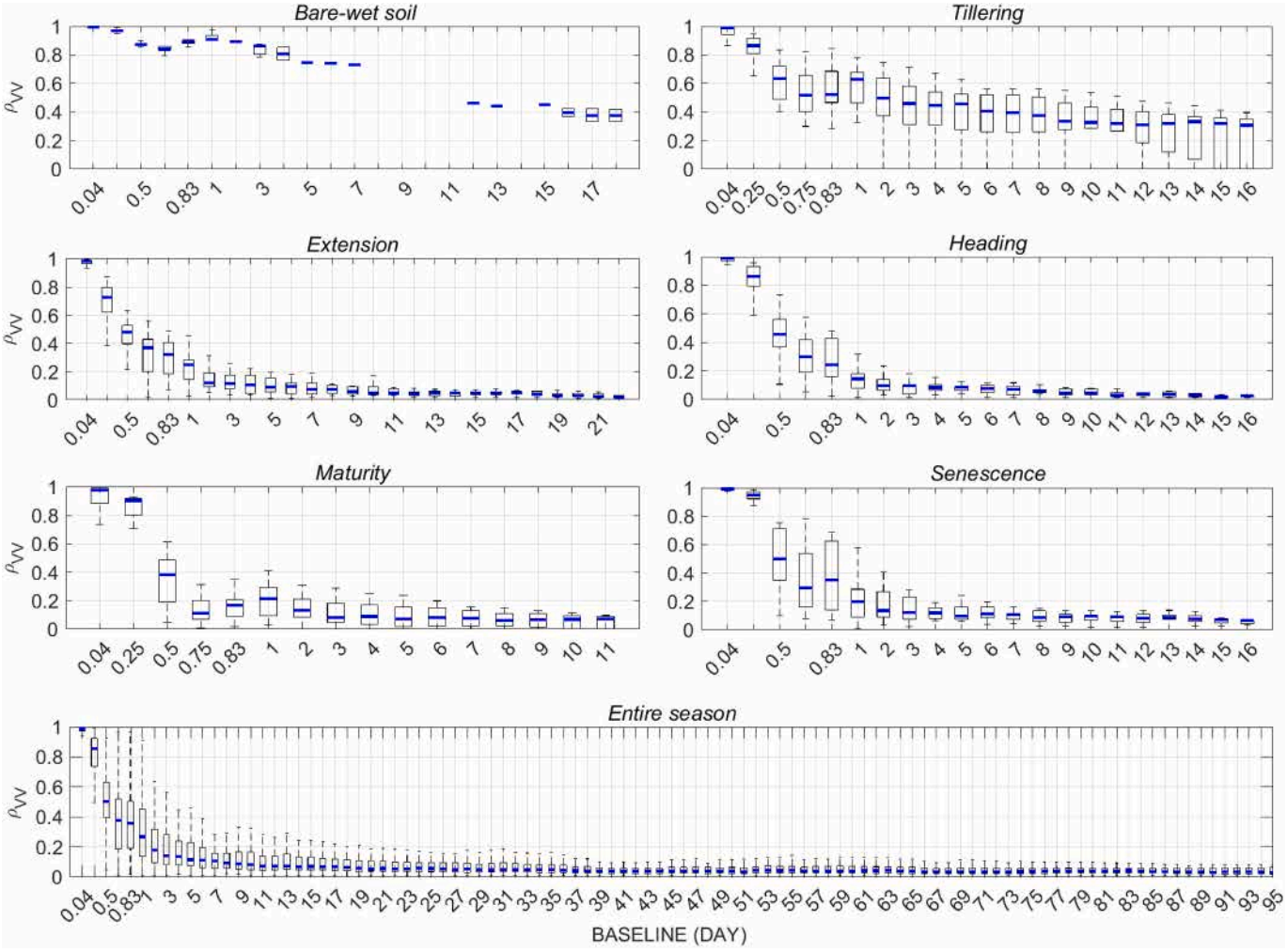

Fig. 10. Boxplots representing the evolution of temporal coherence at 06 h (6:00 a.m.) acquisition time versus temporal baseline in days (0.25 corresponds to 6 h) at VV polarization over the agricultural season.

by temperature, meaning that with thermal inertia, evaporative demand is very low in the morning. By contrast, even very low incoming radiation can stimulate transpiration at sunrise as stomata are strongly sensitive to radiation in the blue wavelength domain that is dominating incoming radiation at dawn (Matthews et al., 2020; Zait et al., 2017). Indeed, with a similar wind levels, the drop of temporal coherence is stronger at dawn than at night.

This study also showed that the effect of SSM on sub-daily coherence is limited for most of the season. This is in agreement with several works (Moeremans and Dautrebande, 2000; Molan and Lu, 2020; Ouaadi et al., 2020b) that have demonstrated the negligible effect of SSM when the vegetation covers the soil, all the more for C-band characterized by a lower penetration depth within the canopy than longer wavelengths. At the sub-daily scale also, results reported by Albinet et al. (2016) show no effect of irrigating a tree on its P-band temporal coherence. However, the lack of sensitivity could also be linked to the high incidence range (45–60°) in this study. By contrast, over bare soil period, an impact of soil watering through irrigation was observed in this study, leading to a decorrelation after the start of the event. This decorrelation related to SSM variations was already observed over bare soils at different frequencies including C-band (Morrison et al., 2011) and L-band (De Zan et al., 2014). Of course, the observed decorrelation in this study, lasting about 1 h, is rather limited because of the drip irrigation technique that water a small fraction of the soil along the plant row. Nevertheless, it is likely that the effect could be stronger for irrigation methods that water a high soil fraction such as the flooding technique for instance. Within this context, this result offers a promising potential of the sub-daily C-band coherence to detect irrigation events at least in the early season when the ground is almost bare. Indeed, irrigation timing and amount are key information to improve irrigation practices in order to rationalize the agricultural water use and are strongly uncertain over large areas at the field scale (Massari et al., 2021).

Likewise, liquid water on the vegetation foliage such as dew impacts the daily dynamic of the temporal coherence. While some authors highlighted an impact on the backscattering coefficient up to 2 dB (Hornbuckle et al., 2010; Khabbazan et al., 2022; Kumar et al., 2013; Vermunt et al., 2020), its effect on the coherence is still to be explored at C-band. Precipitation was shown to disrupt the daily coherence cycles (Hamadi et al., 2014) of trees. Albinet et al. (2016) showed that artificial watering of a tree caused a sharp decrease of P-band coherence thanks to observations carried out over a 10 h period between 08 h and 18 h. In this study, the formation of morning dew has induced a slight increase of coherence lasting about two hours instead of a decreasing trend that was observed in the previously described experiment. The first difference between studies is the wavelength and its interaction with the canopy cover. Indeed, P-band coherence of the tree is very high (above 0.98) because of a longer wavelength and its associated sensitivity to the most stable elements of the tree (the trunk and the biggest branches). In this study, temporal coherence is much more impacted by the movement of scatterers of lower dimension such as wheat leaves as shown by the stronger diurnal cycles. It is also possible that the presence of water on the canopy surface together with a water-vapor saturated air stop

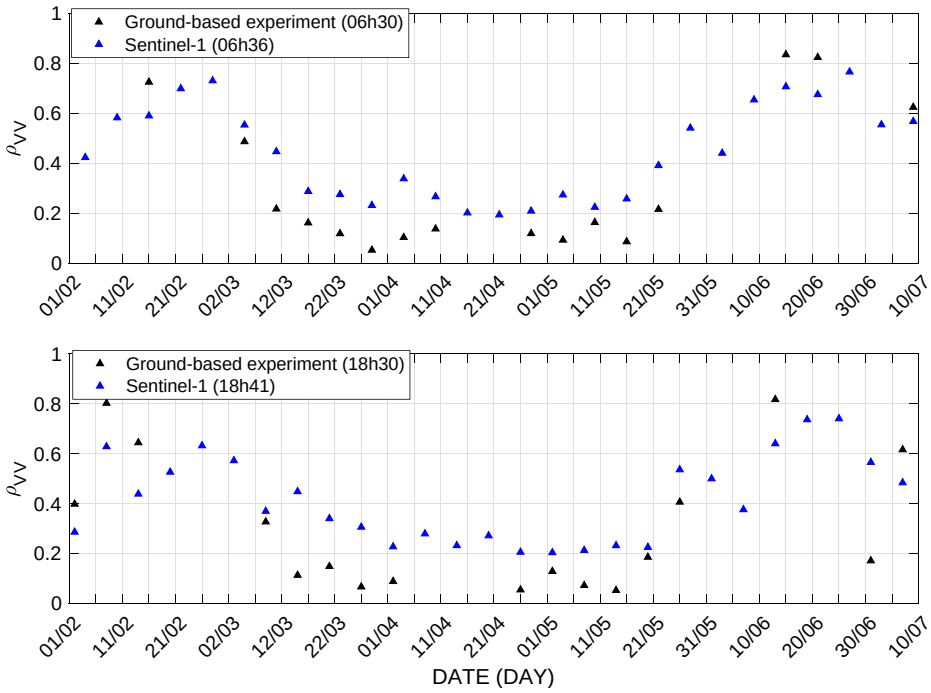

Fig. 11. Time series of the 6-day Sentinel-1 coherence and the ground-based experiment temporal coherence computed at the Sentinel-1 day and time overpass.

transpiration and limiting the water displacement due to root uptake within the plant (Dawson and Goldsmith, 2018; Khabbazan et al., 2022). Stating differently, dew formation is a natural phenomenon that indicates zero water demand from the atmosphere and therefore zero transpiration, in contrast to artificial watering which not only induces dislocation of the scatterers but also occurs in the presence of transpiration. It is likely that the presence of dew stopped transpiration (Gerlein-Safdi et al., 2018; Khabbazan et al., 2022) because of a saturated air at the boundary layer of the leaves and because of the presence of liquid water. This assumption should be further investigated as it could be a supplementary clue that the physiological functioning of the plant is one of the main factor impacting decorrelation during the first hours following sunrise as if transpiration stops, temporal coherence increases. Finally, this sensitivity of coherence to dew could also be an opportunity for the detection of sprinkler irrigation event or rainfall.

By contrast, beyond soil and vegetation water content and above-ground biomass effects, coherence is well known to be impacted by changes in soil roughness (Ouaadi et al., 2020b; Wegmuller and Werner, 1997). This effect could not be analyzed in this study as soil works were carried out before sowing and soil roughness remains stable during the growing season.

Finally, this study also highlights a strong decorrelation during the full development of wheat as temporal coherence values fall beyond 0.2 for baseline above 2 days showing the limits of the sensors actually into orbit such as Sentinel-1 offering at best a 6-day repeat cycle. On tropical forest, experiments showed that high coherence values ($\geq$ 0.8 up to 10 days and $\geq$0.6 up to 30 days) can be obtained at P-band during the dry season for 06 h acquisition time (El Idrissi Essebtey et al., 2021). Hamadi et al. (2017) observed obviously lower values at L-band. At C-band (El Idrissi Essebtey et al., 2019), temporal coherence values remained above 0.2 up to 4 days of baseline. In addition, due to the rapid growth of wheat, different decorrelation rates are observed depending on the considered sub-period of the season. For the 1-day baseline, for example, a gradual decrease in coherence (acquisition time at 06 h) is observed between very low soil cover (NDVI = 0.2) and maturity (NDVI = 0.8). A median value >0.8 up to 4 days is obtained for very low covered soil and a median values >0.4 during tillering. The effect of the coherent contribution from the soil is likely the responsible of the low decorrelation during these early stages as shown by Askne et al. (1997) on a boreal forest. Once the vegetation covers the ground, a very high decorrelation for baselines above 1-day is observed in agreement with the study of El Idrissi Essebtey et al. (2019) carried out at C-band on tropical forest. Similar order of values was observed using the 6-day baseline of Sentinel-1 (high values of coherence about 0.8 at the start of the season and values below 0.4 from extension onwards) such as in the work by Ouaadi et al. (2020b) carried out on wheat fields on the same study area. Villarroya-Carpio et al. (2022) also reported similar results on wheat in Spain using Sentinel-1 with a 6-day baseline. By contrast, lower values were obviously reported by Nasirzadehdizaji et al. (2021) and Barbouchi et al. (2022) given the 12-day baseline on their region of study: maximum values around 0.6 were recorded before sowing and after harvest and values down to 0.1 were observed during full development. Interesting enough, quite similar values were obtained in these studies when comparing different orbits (incidences between 31.5° and 45.6°) in agreement with the results of this study with Sentinel-1 data. Using the ground-based experiment, comparison of the diurnal cycle of three incidence ranges (27–45°, 45–55° and 55°-60°) revealed a slightly higher decorrelation for high incidences, well known to be more sensitive to vegetation. However, the ground-based experiment range of incidence going from 27° to 60° is larger than the range of Sentinel-1 incidence angle. Finally, Villarroya-Carpio et al. (2022) and Nasirzadehdizaji et al. (2021) have also highlighted differences in vegetation monitoring performance between some orbits that was attributed to changes of wind velocity in relation to the time of the satellite overpasses. This suggests that future missions aiming to assess the vegetation hydrological functioning should consider overpass times when wind is minimal.

In the objective of providing some guidance elements to design new innovating instruments able to provide sub-daily C-band data (ESA, 2020; Hu et al., 2021), the results of this study showed that acquisitions should be able to catch the minimum and maximum values of the daily cycle around midnight and after noon around the daily peak of wind velocity. In addition, a much denser sampling during the early morning hours around sunrise would be recommended in order to catch the coherence morning drop.

5. Conclusion

The present study aims to investigate for the first time the diurnal cycle of sub-daily temporal coherence over wheat crops and its relation with plant physiological functioning. Data acquired with 15 min time steps from a C-band ground experiment installed in Morocco during the 2020 season are used. The results show that the temporal coherence computed with a baseline of 15 min exhibits a diurnal cycle that increases with vegetation development. In particular, coherence morning drop is highly correlated with morning evapotranspiration ($r = 0.8$, significant at 99%) when vegetation is in full activity. In contrast, the high wind speeds around 17 h is concomitant with the minimum coherence reached at this time of day with a correlation coefficient of 0.7. Surface soil moisture was found to have a very limited impact on the 15-min coherence diurnal cycle over the season, whereas an abrupt decorrelation is observed on the temporal coherence with baselines from 15-min to 23-h during the bare soil period in response to irrigation events. Dew formation was also found to have an impact on temporal coherence with baselines from 15-min to 23-h during the two hours of its presence. For larger baselines, from 1 to 22 days depending on the season sub-period, the results show strong decorrelation from 2 days onwards when the vegetation is well developed, highlighting the importance of such ground-based experiments to (i) investigate physical processes that occur over short periods of time and (ii) point to the need for future high temporal resolution missions, in particular for the investigation of annual crops which are complex mediums evolving in time.

The outcomes of this study can be explored and enhanced on larger scale with the launch of geostationary satellite missions to develop appropriate methods for monitoring vegetation water use under different climates and vegetation types; in particular, for the early detection of water stress (Ouaadi et al., 2020a; Van Emmerik et al., 2015; Vermunt et al., 2020) in order to improve irrigation scheduling. This could also be investigated by combining radar and thermal data. In this study, the triggered stress was moderate and coincided with a strong wheat growth phase and wind storms, emphasizing the need to schedule another stress experiment under better conditions to better isolate the effect of water stress. The study could also include: (i) a full polarimetric investigation after applying crosstalk correction, and (ii) combining temporal coherence and backscattering coefficient to provide new insights, especially with the use of electromagnetic models (Attema and Ulaby, 1978; Karam et al., 1992; Ulaby et al., 1990) to improve the understanding of the different contributions from different canopy components at the sub-daily scale, and potentially retrieve biophysical variables.

CRediT authorship contribution statement

Nadia Ouaadi: Writing – review & editing, Writing – original draft, Visualization, Software, Methodology, Investigation, Formal analysis, Data curation, Conceptualization. **Lionel Jarlan:** Writing – review & editing, Writing – original draft, Supervision, Investigation, Funding acquisition, Formal analysis, Conceptualization. **Ludovic Villard:** Writing – review & editing, Visualization, Methodology, Investigation, Funding acquisition, Formal analysis, Data curation, Conceptualization. **Adnane Chakir:** Writing – review & editing, Formal analysis, Data curation. **Saïd Khabba:** Writing – review & editing, Investigation, Formal analysis. **Pascal Fanise:** Formal analysis, Data curation. **Mohamed Kasbani:** Writing – review & editing, Data curation. **Zoubair Rafi:** Writing – review & editing. **Valerie Le Dantec:** Writing – review & editing, Formal analysis. **Jamal Ezzahar:** Writing – review & editing. **Pierre-Louis Frison:** Writing – review & editing, Visualization, Methodology, Funding acquisition, Formal analysis, Conceptualization.

Declaration of competing interest

The authors declare that they have no known competing financial interests or personal relationships that could have appeared to influence the work reported in this paper.

Data availability

Data will be made available on request.

Acknowledgment

The experiment is conducted within the frame of the CNES-TOSCA MOCTAR project with the support of the International Joint Laboratory TREMA (https://www.lmi-trema.ma/). N.O. was funded by the ANR-19-CE01-0017 HILIAISE project. The authors thank the financial support of the projects ERANET-MED CHAAMS and Rise-H2020-ACCWA. The authors are grateful to Theia for producing and distributing Sentinel-2 images corrected from atmospheric effects and to ESA for providing Sentinel-1 products free of charge. Finally, we would like to acknowledge Dr. Omar Rafi, the owner of the private farm for his long-time support for our research activities.

Appendix A. Supplementary data

Supplementary data to this article can be found online at https://doi.org/10.1016/j.rse.2024.114059.

References

Abourida, A., Simonneaux, V., Errouane, S., Sighir, F., Berjami, B., Sgir, F., 2008. Estimation des volumes d'eau pompés dans la nappe pour l'irrigation (Plaine du Haouz, Marrakech, Maroc). Comparaison d'une méthode statistique et d'une méthode basée sur l'utilisation de données de télédétection. J. Water Sci. 21, 489–501.

Albinet, C., Borderies, P., Floury, N., Pottier, E., 2016. Measure of temporal variation of P-band radar cross section and temporal coherence of a temperate tree. IEEE Trans. Geosci. Remote Sens. 54, 6255–6264. https://doi.org/10.1109/TGRS.2016.2565384.

Al-Kahachi, N., Tienda, C., Younis, M., 2014. Polarimetric cross-talk in SAR system induced by antenna cross-pol pattern. In: Proceedings of the European Conference on Synthetic Aperture Radar. EUSAR, pp. 1365–1368.

Allen, R.G., Pereira, L.S., Raes, D., Smith, M., 1998. Crop Evapotranspiration—Guidelines for Computing Crop Water Requirements, FAO Irrigation and Drainage Paper No. 56. FAO, ROME, Italy.

Allen, R.G., Pereira, L.S., Howell, T.A., Jensen, M.E., 2011. Evapotranspiration information reporting: I. Factors governing measurement accuracy. Agric. Water Manag. https://doi.org/10.1016/j.agwat.2010.12.015.

Aouade, G., Ezzahar, J., Amenzou, N., Er-Raki, S., Benkaddour, A., Khabba, S., Jarlan, L., 2016. Combining stable isotopes, Eddy covariance system and meteorological measurements for partitioning evapotranspiration, of winter wheat, into soil evaporation and plant transpiration in a semi-arid region. Agric. Water Manag. 177, 181–192. https://doi.org/10.1016/j.agwat.2016.07.021.

Askne, J.I.H., Dammert, P.B.G., Ulander, L.M.H., Smith, G., 1997. C-band repeat-pass interferometric SAR observations of the forest. Doktorsavhandl. Chalmers Tek. Hogsk. 35, 25–35.

Attema, E.P.W., Ulaby, F.T., 1978. Vegetation modeled as a water cloud. Radio Sci. 13, 357–364. https://doi.org/10.1029/RS013i002p00357.

Barbouchi, M., Chaabani, C., Cheikh M'Hamed, H., Abdelfattah, R., Lhissou, R., Chokmani, K., Ben Aissa, N., Annabi, M., Bahri, H., 2022. Wheat water deficit monitoring using synthetic aperture radar backscattering coefficient and interferometric coherence. Agric. 12, 1–14. https://doi.org/10.3390/agriculture12071032.

Birrer, I., Bracalente, E., Dome, G.J., Sweet, J., Berthold, G., 1982. σ° signature of the Amazon rain Forest obtained from the Seasat Scatterometer. IEEE Trans. Geosci. Remote Sens. 20, 11–17. https://doi.org/10.1109/TGRS.1982.4307513.

Blaes, X., Defourny, P., 2003. Retrieving crop parameters based on tandem ERS 1 / 2 interferometric coherence images. Remote Sens. Environ. 88, 374–385. https://doi.org/10.1016/j.rse.2003.08.008.

Brakke, T.W., Kanemasu, E.T., Steiner, J.L., Ulaby, F.T., Wilson, E., 1981. Microwave radar response to canopy moisture, leaf-area index, and dry weight of wheat, corn, and sorghum. Remote Sens. Environ. 11, 207–220. https://doi.org/10.1016/0034-4257(81)90020-1.

Capella Space. n.d. URL http://www.capellaspace.com.

Chen, R., Xiong, X., Cheng, W., 2021. Root characteristics of spring wheat under drip irrigation and their relationship with aboveground biomass and yield. Sci. Rep. 11, 4913. https://doi.org/10.1038/s41598-021-84208-7.

Dawson, T.E., Goldsmith, G.R., 2018. The value of wet leaves. New Phytol. 219, 1156–1169. https://doi.org/10.1111/nph.15307.
De Zan, F., Parizzi, A., Prats-Iraola, P., López-dekker, P., 2014. A SAR interferometric model for soil moisture. IEEE Trans. Geosci. Remote Sens. 52, 418–425. https://doi.org/10.1109/TGRS.2013.2241069.
van Dijk, A., Moene, A.F., de Bruin, H.A.R., 2004. The Principles of Surface Flux Physics: Theory, Practice and Description of the ECPACK Library. Internal Report 2004/1,. Meteorology and Air Quality Group, the Netherlands.
El Idrissi Essebtey, S., Villard, L., Borderies, P., Koleck, T., Monvoisin, J.P., Burban, B., Le Toan, T., 2019. Temporal decorrelation of tropical dense Forest at C-band: first insights from the TropiScat-2 experiment. IEEE Geosci. Remote Sens. Lett. 1–5. https://doi.org/10.1109/lgrs.2019.2937382.
El Idrissi Essebtey, S., Villard, L., Borderies, P., Koleck, T., Burban, B., Le Toan, T., 2021. Long-term trends of P-band temporal decorrelation over a tropical dense Forest-experimental results for the BIOMASS Mission. IEEE Trans. Geosci. Remote Sens. 60, 1–15. https://doi.org/10.1109/TGRS.2021.3082395.
ESA, 2012. BIOMASS: Report for Mission Selection, an Earth Explorer to Observe Forest Biomass, SP-132. ed. ESA, Noordwijk, The Netherlands.
ESA, 2020. Earth Explorer 10 Candidate Mission Hydroterra: Report for Assessment ESA. Noordwijk, The Netherlands.
Foley, J.A., Ramankutty, N., Brauman, K.A., Cassidy, E.S., Gerber, J.S., Johnston, M., Mueller, N.D., O'Connell, C., Ray, D.K., West, P.C., Balzer, C., Bennett, E.M., Carpenter, S.R., Hill, J., Monfreda, C., Polasky, S., Rockström, J., Sheehan, J., Siebert, S., Tilman, D., Zaks, D.P.M., 2011. Solutions for a cultivated planet. Nature 478, 337–342. https://doi.org/10.1038/nature10452.
Freeman, A., Shen, Y., Werner, C.L., 1990. Polarimetric SAR calibration experiment using active radar calibrators. IEEE Trans. Geosci. Remote Sens. 28, 224–240. https://doi.org/10.1109/36.46702.
Friesen, J., Winsemius, H.C., Beck, R., Scipal, K., Wagner, W., Van De Giesen, N., 2007. Spatial and seasonal patterns of diurnal differences in ERS scatterometer soil moisture data in the Volta basin, West Africa. IAHS-AISH Publ. 47–55.
Frison, P.L., Fruneau, B., Kmiha, S., Soudani, K., Dufrêne, E., Le Toan, T., Koleck, T., Villard, L., Mougin, E., Rudant, J.P., 2018. Potential of Sentinel-1 data for monitoring temperate mixed forest phenology. Remote Sens. 10, 2049. https://doi.org/10.3390/rs10122049.
Frolking, S., Milliman, T., Palace, M., Wisser, D., Lammers, R., Fahnestock, M., 2011. Tropical forest backscatter anomaly evident in SeaWinds scatterometer morning overpass data during 2005 drought in Amazonia. Remote Sens. Environ. 115, 897–907. https://doi.org/10.1016/J.RSE.2010.11.017.
Gates, D.M., 1991. Water relations of forest trees. EEE Trans. Geosci. Remote Sens. 29, 836–842.
Gerlein-Safdi, C., Koohafkan, M.C., Chung, M., Rockwell, F.E., Thompson, S., Caylor, K. K., 2018. Dew deposition suppresses transpiration and carbon uptake in leaves. Agric. For. Meteorol. 259, 305–316. https://doi.org/10.1016/j.agrformet.2018.05.015.
Hamadi, A., Albinet, C., Borderies, P., Koleck, T., Villard, L., Ho Tong Minh, D., Le Toan, T., 2014. Temporal survey of polarimetric P-band scattering of tropical forests. IEEE Trans. Geosci. Remote Sens. 52, 4539–4547. https://doi.org/10.1109/TGRS.2013.2282357.
Hamadi, A., Borderies, P., Albinet, C., Koleck, T., Villard, L., Ho Tong Minh, D., Le Toan, T., Burban, B., 2015. Temporal coherence of tropical forests at P-band: dry and rainy seasons. IEEE Geosci. Remote Sens. Lett. 12, 557–561. https://doi.org/10.1109/LGRS.2014.2350513.
Hamadi, A., Villard, L., Borderies, P., Albinet, C., Koleck, T., Le Toan, T., 2017. Comparative analysis of temporal decorrelation at P-band and low L-band frequencies using a tower-based Scatterometer over a tropical Forest. IEEE Geosci. Remote Sens. Lett. 14, 1918–1922. https://doi.org/10.1109/LGRS.2017.2731658.
Herzog, K.M., Häsler, R., Thum, R., 1995. Diurnal changes in the radius of a subalpine Norway spruce stem: their relation to the sap flow and their use to estimate transpiration. Trees Struct. Funct. 10, 94–101. https://doi.org/10.1007/BF00192189.
Hornbuckle, B.K., Rowlandson, T.L., Russell, E., Kaleita, A., Logsdon, S., Kruger, A., Yueh, S., De Roo, R.D., 2010. How does dew affect L-band backscatter? Analysis of pals data at the Iowa validation site and implications for SMAP. Int. Geosci. Remote Sens. Symp. 4835–4838 https://doi.org/10.1109/IGARSS.2010.5650792.
Hu, C., Chen, Z., Li, Y., Dong, X., Hobbs, S., 2021. Research progress on geosynchronous synthetic aperture radar. Fundam. Res. 1, 346–363. https://doi.org/10.1016/j.fmre.2021.04.008.
ICEYE. n.d. URL http://www.iceye.com.
Ihuoma, S.O., Madramootoo, C.A., 2017. Recent advances in crop water stress detection. Comput. Electron. Agric. 141, 267–275. https://doi.org/10.1016/j.compag.2017.07.026.
Jackson, R.D., Idso, S.B., Reginato, R.J., Pinter, P.J., 1981. Canopy temperature as a crop water stress indicator. Water Resour. Res. 17, 1133–1138. https://doi.org/10.1029/WR017I004P01133.
Jarlan, L., Khabba, S., Er-Raki, S., Le Page, M., Hanich, L., Fakir, Y., Merlin, O., Mangiarotti, S., Gascoin, S., Ezzahar, J., Kharrou, M.H., Berjamy, B., Saaïdi, A., Boudhar, A., Benkaddour, A., Laftouhi, N., Abaoui, J., Tavernier, A., Boulet, G., Simonneaux, V., Driouech, F., El Adnani, M., El Fazziki, A., Amenzou, N., Raibi, F., El Mandour, H., Ibouh, H., Le Dantec, V., Habets, F., Tramblay, Y., Mougenot, B., Leblanc, M., El Faïz, M., Drapeau, L., Coudert, B., Hagolle, O., Filali, N., Belaqziz, S., Marchane, A., Szczypta, C., Toumi, J., Diarra, A., Aouade, G., Hajhouji, Y., Nassah, H., Bigeard, G., Chirouze, J., Boukhari, K., Abourida, A., Richard, B., Fanise, P., Kasbani, M., Chakir, A., Zribi, M., Marah, H., Naimi, A., Mokssit, A., Kerr, Y., Escadafal, R., 2015. Remote sensing of water resources in semi- arid Mediterranean areas : the joint international laboratory TREMA. Int. J. Remote Sens. 36, 4879–4917. https://doi.org/10.1080/01431161.2015.1093198.
Karam, M.A., Fung, A.K., Lang, R.H., Chauhan, N.S., 1992. Microwave scattering model for layered vegetation. IEEE Trans. Geosci. Remote Sens. 30, 767–784. https://doi.org/10.1109/36.158872.
Khabbazan, S., Steele-Dunne, S.C., Vermunt, P., Judge, J., Vreugdenhil, M., Gao, G., 2022. The influence of surface canopy water on the relationship between L-band backscatter and biophysical variables in agricultural monitoring. Remote Sens. Environ. 268, 112789 https://doi.org/10.1016/j.rse.2021.112789.
Kumar, S.D., Rao, S.S., Sharma, J.R., 2013. Radar vegetation index as an alternative to NDVI for monitoring of Soyabean and cotton. Indian Cartogr. 33, 91–96.
Kunz, L.B., Long, D.G., 2005. Calibrating SeaWinds and QuikSCAT scatterometers using natural land targets. IEEE Geosci. Remote Sens. Lett. 2, 182–186. https://doi.org/10.1109/LGRS.2004.842468.
Lavalle, M., Simard, M., Hensley, S., 2012. A temporal decorrelation model for polarimetric radar interferometers. IEEE Trans. Geosci. Remote Sens. 50, 2880–2888. https://doi.org/10.1109/TGRS.2011.2174367.
Lawrence, M.G., 2005. The relationship between relative humidity and the dewpoint temperature in moist air: a simple conversion and applications. Bull. Am. Meteorol. Soc. 86, 225–233. https://doi.org/10.1175/BAMS-86-2-225.
Le Page, M., Toumi, J., Khabba, S., Hagolle, O., Tavernier, A., Hakim Kharrou, M., Er-Raki, S., Huc, M., Kasbani, M., El Moutamanni, A., Yousfi, M., Jarlan, L., 2014. A life-size and near real-time test of irrigation scheduling with a sentinel-2 like time series (SPOT4-Take5) in Morocco. Remote Sens. 6, 11182–11203. https://doi.org/10.3390/rs61111182.
Leal Filho, W., Totin, E., Franke, J.A., Andrew, S.M., Abubakar, I.R., Azadi, H., Nunn, P. D., Ouweneel, B., Williams, P.A., Simpson, N.P., 2022. Understanding responses to climate-related water scarcity in Africa. Sci. Total Environ. 806, 150420 https://doi.org/10.1016/j.scitotenv.2021.150420.
Long, D.G., Skouson, G.B., 1996. Calibration of spaceborne scatterometers using tropical rain forests. lEEE Trans. Geosci. Remote Sens. 34.
Massari, C., Modanesi, S., Dari, J., Gruber, A., M., G.J, Lannoy, D., Girotto, M., Quintana-Seguí, P., Le Page, M., Jarlan, L., Zribi, M., Ouaadi, N., Vreugdenhil, M., Zappa, L., Dorigo, W., Wolfgang, W., Brombacher, J., Pelgrum, H., Jaquot, P., Freeman, V., Volden, E., Prieto, D.F., Tarpanelli, A., Barbetta, S., Brocca, L., 2021. A review of irrigation information retrievals from space and their utility for users. Remote Sens. 13 https://doi.org/10.3390/rs13204112.
Matthews, J.S.A., Vialet-Chabrand, S., Lawson, T., 2020. Role of blue and red light in stomatal dynamic behaviour. J. Exp. Bot. 71, 2253–2269. https://doi.org/10.1093/jxb/erz563.
Mcdonald, K.C., Zimmermann, R., Kimball, J.S., 2002. Diurnal and spatial variation of xylem dielectric constant in Norway spruce (Picea abies [L.] karst.) as related to microclimate, xylem sap flow, and xylem chemistry. IEEE Trans. Geosci. Remote Sens. 40, 2063–2082. https://doi.org/10.1109/TGRS.2002.803737.
MedECC, 2020. Climate and Environmental Change in the Mediterranean Basin.
Mestre-Quereda, A., Lopez-Sanchez, J.M., Vicente-Guijalba, F., Jacob, A.W., Engdahl, M. E., 2020. Time-series of Sentinel-1 interferometric coherence and backscatter for crop-type mapping. IEEE J. Sel. Top. Appl. Earth Obs. Remote Sens. 13, 4070–4084. https://doi.org/10.1109/JSTARS.2020.3008096.
Moeremans, B., Dautrebande, S., 2000. Soil moisture evaluation by means of multi-temporal ERS SAR PRI images and interferometric coherence. J. Hydrol. 234, 162–169. https://doi.org/10.1016/S0022-1694(00)00251-1.
Molan, Y.E., Lu, Z., 2020. Can InSAR coherence and closure phase be used to estimate soil moisture changes? Remote Sens. 12 https://doi.org/10.3390/RS12091511.
Morrison, K., Bennett, J.C., Nolan, M., Menon, R., 2011. Laboratory measurement of the DInSAR response to spatiotemporal variations in soil moisture - IEEE journals & magazine. IEEE Trans. Geosci. Remote Sens. 49, 3815–3823. https://doi.org/10.1109/TGRS.2011.2132137.
Nasirzadehdizaji, R., Cakir, Z., Balik Sanli, F., Abdikan, S., Pepe, A., Calò, F., 2021. Sentinel-1 interferometric coherence and backscattering analysis for crop monitoring. Comput. Electron. Agric. 185 https://doi.org/10.1016/j.compag.2021.106118.
Ouaadi, N., Jarlan, L., Ezzahar, J., Khabba, S., Le Dantec, V., Rafi, Z., Zribi, M., Frison, P.-L., 2020a. Water stress detection over irrigated wheat crops in semi-arid areas using the diurnal differences of Sentinel-1 backscatter. In: 2020 IEEE Mediterranean and Middle-East Geoscience and Remote Sensing Symposium (M2GARSS). IEEE, Tunis, Tunisia, pp. 306–309. https://doi.org/10.1109/m2garss47143.2020.9105171.
Ouaadi, N., Jarlan, L., Ezzahar, J., Zribi, M., Khabba, S., Bouras, E., Bousbih, S., Frison, P., 2020b. Monitoring of wheat crops using the backscattering coe ffi cient and the interferometric coherence derived from Sentinel-1 in semi-arid areas. Remote Sens. Environ. 251, 112050 https://doi.org/10.1016/j.rse.2020.112050.
Ouaadi, N., Ezzahar, J., Khabba, S., Er-Raki, S., Chakir, A., Ait Hssaine, B., Le Dantec, V., Rafi, Z., Beaumont, A., Kasbani, M., Jarlan, L., 2021. C-band radar data and in situ measurements for the monitoring of wheat crops in a semi-arid area (center of Morocco). Earth Syst. Sci. Data 13, 3707–3731. https://doi.org/10.5194/essd-13-3707-2021.
Ouaadi, N., Jarlan, L., Khabba, S., Le Page, M., Chakir, A., Er-raki, S., Frison, P.L., 2023. Are the C-band backscattering coefficient and interferometric coherence suitable substitutes of NDVI for the monitoring of the FAO-56 crop coefficient ? Agric. Water Manag. 282, 108276 https://doi.org/10.1016/j.agwat.2023.108276.
Plant, Z., Carmi, A., Grava, A., 1988. Cotton growth and production under drip-irrigation restricted soil wetting. Irrig. Sci. 9, 143–156. https://doi.org/10.1007/BF00262356.
Quegan, S., 1994. A unified algorithm for phase and cross-talk calibration of Polarimetric data-theory and observations. IEEE Trans. Geosci. Remote Sens. 32, 89–99. https://doi.org/10.1109/36.285192.

Rafi, Z., 2020. Détection et suivi du fonctionnement hydrique d'une culture de blé en milieu semi-aride. Toulouse III University, p. 140 thesis report,.

Stefan, V.G., Merlin, O., Er-Raki, S., Escorihuela, M.J., Khabba, S., 2015. Consistency between in situ, model-derived and high-resolution-image-based soil temperature endmembers: towards a robust data-based model for multi-resolution monitoring of crop evapotranspiration. Remote Sens. Vol. 7, 10444–10479. https://doi.org/10.3390/RS70810444.

Stringer, L.C., Mirzabaev, A., Benjaminsen, T.A., Harris, R.M.B., Jafari, M., Lissner, T.K., Stevens, N., Tirado-von der Pahlen, C., 2021. Climate change impacts on water security in global drylands. One Earth 4, 851–864. https://doi.org/10.1016/j.oneear.2021.05.010.

Ulaby, F.T., Moore, R.K., Fung, A.K., 1986. Microwave Remote Sensing: Active and Passive, Volume III-from Theory to Applications.

Ulaby, F.T., Sarabandi, K., McDonald, K., Whitt, M., Craig Dobson, M., 1990. Michigan microwave canopy scattering model. Int. J. Remote Sens. 11, 1223–1253. https://doi.org/10.1080/01431169008955090.

United Nations Children''s Fund (UNICEF) and World Health Organization, 2019. Special focus on inequalities. In: Progress on Household Drinking Water, Sanitation and Hygiene, 2000–2017. New York.

Van Emmerik, T., Steele-Dunne, S.C., Judge, J., Van De Giesen, N., 2015. Impact of diurnal variation in vegetation water content on radar backscatter from maize during water stress. IEEE Trans. Geosci. Remote Sens. 53, 3855–3869. https://doi.org/10.1109/TGRS.2014.2386142.

Van Emmerik, T., Steele-Dunne, S.C., Judge, J., Van De Giesen, N., 2017. Dielectric response of corn leaves to water stress. IEEE Geosci. Remote Sens. Lett. 14, 8–12. https://doi.org/10.1109/LGRS.2016.2606662.

Van Zyl, J.J., 1990. Calibration of Polarimetric radar images using only image parameters and trihedral corner reflector responses. IEEE Trans. Geosci. Remote Sens. 28, 337–348. https://doi.org/10.1109/36.54360.

Vermunt, P.C., Khabbazan, S., Steele-Dunne, S.C., Judge, J., Monsivais-Huertero, A., Guerriero, L., Liu, P.W., 2020. Response of subdaily L-band backscatter to internal and surface canopy water dynamics. IEEE Trans. Geosci. Remote Sens. 1–16 https://doi.org/10.1109/TGRS.2020.3035881.

Villarroya-Carpio, A., Lopez-Sanchez, J.M., Engdahl, M.E., 2022. Sentinel-1 interferometric coherence as a vegetation index for agriculture. Remote Sens. Environ. 280, 113208 https://doi.org/10.1016/j.rse.2022.113208.

Wegmuller, U., Werner, C., 1997. Retrieval of vegetation parameters with SAR interferometry. IEEE Trans. Geosci. Remote Sens. 35, 18–24. https://doi.org/10.1109/36.551930.

Zait, Y., Shapira, O., Schwartz, A., 2017. The effect of blue light on stomatal oscillations and leaf turgor pressure in banana leaves. Plant Cell Environ. 40, 1143–1152. https://doi.org/10.1111/pce.12907.